Title
Chapter 7 Brain metastases: neuroimaging

Author
Pope, Whitney B

Publication Date
2018

DOI
10.1016/b978-0-12-811161-1.00007-4

Peer reviewed

HHS Public Access

Author manuscript

Handb Clin Neurol. Author manuscript; available in PMC 2018 August 31.

Published in final edited form as:

Handb Clin Neurol. 2018 ; 149: 89–112. doi:10.1016/B978-0-12-811161-1.00007-4.

Brain metastases: neuroimaging

WHITNEY B. POPE*

Department of Radiological Sciences, David Geffen School of Medicine, University of California, Los Angeles, CA, United States

Abstract

Magnetic resonance imaging (MRI) is the cornerstone for evaluating patients with brain masses such as primary and metastatic tumors. Important challenges in effectively detecting and diagnosing brain metastases and in accurately characterizing their subsequent response to treatment remain. These difficulties include discriminating metastases from potential mimics such as primary brain tumors and infection, detecting small metastases, and differentiating treatment response from tumor recurrence and progression. Optimal patient management could be benefited by improved and well-validated prognostic and predictive imaging markers, as well as early response markers to identify successful treatment prior to changes in tumor size. To address these fundamental needs, newer MRI techniques including diffusion and perfusion imaging, MR spectroscopy, and positron emission tomography (PET) tracers beyond traditionally used 18-fluorodeoxyglucose are the subject of extensive ongoing investigations, with several promising avenues of added value already identified. These newer techniques provide a wealth of physiologic and metabolic information that may supplement standard MR evaluation, by providing the ability to monitor and characterize cellularity, angiogenesis, perfusion, pH, hypoxia, metabolite concentrations, and other critical features of malignancy. This chapter reviews standard and advanced imaging of brain metastases provided by computed tomography, MRI, and amino acid PET, focusing on potential biomarkers that can serve as problem-solving tools in the clinical management of patients with brain metastases.

INTRODUCTION

Magnetic resonance (MR) replaced computed tomography (CT) as the imaging modality of choice for brain metastases in the 1980s. Since that time capabilities of modern MR scanners have been greatly expanded, due to improvements in hardware, including more powerful gradients and increasing magnetic field, as well as improvements in software, including the development of additional pulse sequences and more advanced image postprocessing and quantitative data extraction and analysis capabilities. Now MR scanners can be used to acquire a wealth of information on metastases or other intracranial pathologies that go far beyond anatomy to include both metabolic as well as physiologic information by diffusion, perfusion, MR spectroscopic, and other more recently developed imaging techniques. Positron emission tomography (PET) scanning also has advanced with the more widespread

*Correspondence to: Whitney B. Pope, Department of Radiological Sciences, David Geffen School of Medicine at UCLA, 757 Westwood Plaza, 1621E, Los Angeles CA 90066, United States. Tel: +1-310-267-9783, wpope@mednet.ucla.edu.

adoption of amino acid tracers replacing traditional 18-fluorodeoxyglucose (FDG), with improvements in signal-to-noise ratio and diagnostic specificity.

How these newer imaging data can be quantified and developed into robust biomarkers that improve clinical decision making and patient outcomes is a broad topic with extensive ongoing development. This review covers the fundamentals of imaging brain metastases as well as recent progress in successfully employing advanced imaging biomarkers as problem-solving tools in patient care.

CT AND MR: STANDARD IMAGING, LOCATION, GENERAL APPEARANCE

MR imaging (MRI), first applied clinically in the 1980s, almost immediately supplanted CT as the imaging method of choice for patients with brain tumors, including metastatic disease, and for following response to treatment (Graif et al., 1985; Patel et al., 2012). However, CT continues to have a role in brain tumor imaging, particularly as a screening exam for patients with acute neurologic deficits. Even nonenhanced CT can detect neurosurgical emergencies that require immediate intervention such as mass effect, hydrocephalus, and hemorrhage, as modern multislice CT scanners can acquire and reconstruct images of the brain in a matter of seconds. Additionally some patients cannot have MRI due to pacemakers or other contraindications. Therefore, in clinical practice, the first imaging of a patient with brain metastasis may utilize CT.

Sensitivity for small tumors is quite low on CT, however; sometimes the only finding will be low density indicative of vasogenic edema with no underlying lesion visible. Visibility of metastases on CT is improved with iodine-based contrast injection (Lin et al., 1976). However, sensitivity on even contrast-enhanced CT exams remains well below that of MRI (Fig. 7.1) (Seute et al., 2008). CT also has the disadvantage of relying on ionizing radiation, and minimizing patient exposure to radiation is desirable (Kamalian et al., 2016). Conversely, CT does have an advantage over MRI in revealing fine bony detail, particularly with the use of bone kernel for reconstruction of raw data. Therefore the extent of bony destruction from calvarial metastases can usually be better evaluated with CT, given its ability to demonstrate even small areas of bone disruption (Maroldi et al., 2005).

Of cranial and intracranial locations potentially involved by metastatic disease, parenchymal metastases are the most common. But metastases develop in a wide array of nonparenchymal areas, including the inner or outer table of the calvarium, the calvarial diploic space, the meninges (both dura and leptomeninges), and associated brain structures, including the choroid plexus and pituitary stalk and gland. The dura can be the primary site of a metastatic focus, but the dura is also often involved due to direct extension of overlying calvarial metastases. The leptomeninges are involved in carcinomatosis – diffuse involvement of the meninges by malignant cells, potentially spread through the cerebrospinal fluid (CSF). In general, contrast-enhanced MRI is the modality of choice for assessing metastases to these regions due to better tissue contrast and detail and the plethora of MRI sequences that are now available to characterize intracranial lesions (Maroldi et al., 2005; Barajas and Cha, 2012).

MRI provides excellent fine detail and anatomic localization of brain metastases. Parenchymal metastases are typically iso- to hypointense to brain on T1-weighted images, and variable in intensity on T2-weighted images. They tend to be roughly spherical in shape. Metastases often are surrounded by vasogenic edema, which is high signal on T2 and low on T1-weighted images. Edema can often be quite extensive relative to the size of the underlying tumor. Edema typically is confined to the white matter, sparing the overlying cortex. Involvement of the cortex should spur the search for other pathologies such as a primary brain tumor.

Detection of edema can be enhanced with fluid-attenuated inversion recovery (FLAIR) imaging, which suppresses T2-hyperintensity associated with CSF in the ventricles and CSF surrounding the brain. Since metastases lack the normal blood–brain barrier, they usually avidly enhance on postcontrast T1 images. The enhancement may be solid, or peripheral. A peripheral enhancement pattern is more likely as metastases grow in size and outstrip their available blood supply, leading to central necrosis (Smirniotopoulos et al., 2007). Nonenhancing metastases are rare (Elster and Chen, 1992).

In general most parenchymal metastases are visible as foci of FLAIR hyperintensity, including small lesions (Okubo et al., 1998). Conversely, sometimes leptomeningeal or dural metastases will be readily apparent only on postcontrast images and not FLAIR images, although the reverse also is possible (Singh et al., 2000). The presence of calcification, hemorrhage, and cystic components impacts the appearance of metastasis on many common MRI sequences. Calcification, which is hyperdense (bright) on CT, can be high signal on T1 and low on T2 when imaged with MR. Hemorrhage has variable appearance on MRI that evolves over time.

Recent, but not hyperacute, blood tends to be bright on T1-weighted images. Thus intrinsic (precontrast) T1 hyperintensity should raise the possibility of a hemorrhagic component (Zhang et al., 2009). Other features of metastases also can result in intrinsic T1 hyperintensity, including melanin, as can be seen in melanoma metastases (Isiklar et al., 1995). Cystic metastases will be low on T1 and very bright on T2, with the T2 signal intensity approaching that of CSF. Conversely, mucinous metastases may demonstrate central low T2 signal intensity (Egelhoff et al., 1992).

Diffusion-weighted imaging (DWI) has become routine for most clinical MR acquisitions. On diffusion imaging metastases typically show increased diffusion, but this is not always the case. Mucinous and other tumors (breast, colon, testicular, and small and nonsmall cell lung carcinoma) can occasionally show some degree of restricted diffusion, and thus will be bright on DWI, which can lead to ambiguity in differential diagnosis, as discussed below (Fig. 7.2) (Geijer and Holtas, 2002; Bukte et al., 2005; Hayashida et al., 2006).

ENHANCING DETECTION OF SMALL METASTASES

MR has higher sensitivity for the detection of small metastases than CT or even CT/PET (Seute et al., 2008; Krüger et al., 2010). However, sensitivity on MR is variable, as many details of the MR acquisition can impact performance. Since stereotactic radiosurgery (SRS)

protocols and other treatment decisions are based on the location and number of even small metastases, their detection is a clinical concern.

Multiple gadolinium-based contrast agents (GBCA) are available and approved by regulatory bodies around the world for use in clinical applications of MRI. The agents can vary in biophysical properties, including "T1 relaxivity." When other variables are held constant, increasing T1 relaxivity results in greater signal-to-noise ratio on postcontrast exams (i.e., more avid enhancement). For instance, gadobenate dimeglumine has higher relaxivity than gadobutrol, and at the same dose (0.1 mmol/kg body weight) results in improved contrast to noise of brain tumors (Seidl et al., 2012). Many of the GBCA have been compared "head to head," but the outcome may be dependent on dosing and field strength and also impacted by safety profiles (Anzalone et al., 2013).

Increasing GBCA dose appears to increase sensitivity, particularly for small (< 5 mm) lesions, but at the risk of increased false-positive results (Togao et al., 2014). Similarly, increasing MRI field strength also improves metastasis detection. When these variables are combined the gains are substantial. For instance, in a study of 22 patients with suspected brain metastases, the number of lesions detected increased from 70 (1.5 T, single dose) to 84 (3.0 T, triple dose) (Ba-Ssalamah et al., 2003). Contrast dose appeared to have greater impact than field strength, although half-dose contrast at 3.0 T is reportedly superior to full dose at 1.5 T based on measurements of contrast-to-noise ratios (Krautmacher et al., 2005). Ultra-high field strength magnets of 7T may also allow for better lesion detection, even when contrast dose is reduced (Noebauer-Huhmann et al., 2015). Due to concerns about the association of GBCA and the development of nephrogenic systemic fibrosis, higher doses of gadolinium are now generally avoided. Indeed, the US Food and Drug Administration specifically counsels against the use of higher GBCA doses (http://www.fda.gov/Drugs/DrugSafety/ucm142884.htm; Fraum et al., 2017).

Another potential method to enhance detection of metastases is to increase the time delay between contrast injection and acquisition of T1-weighted images. For instance, a time delay of 15 minutes after contrast injection results in at least one additional lesion being detected in 43% of patients (Kushnirsky et al., 2016). Resultant radiation tumor treatment volumes also increase with time delay. Time-delayed imaging may be particularly advantageous in the posterior circulation (Cohen-Inbar et al., 2016). A postinjection delay of 20 minutes appears optimal for maximizing the detection of small lesions (< 10 mm diameter) (Yuh et al., 1995). However, time delay increases time of study acquisition and diminishes scanner throughput, potentially increasing cost as well as patient inconvenience, which may help explain why this methodology is currently not widely adopted.

There are a variety of T1 sequences to choose from for a given MR application. These sequences can be of variable slice thickness and often incorporate a gap between slices, particularly for spin echo or turbo spin echo acquisitions. Alternatively, image acquisition can be volumetric, that is, without a gap, yielding an isometric sampling of the data, so that images can be reconstructed in any plane without loss of detail. Such acquisitions typically have a slice thickness of 1–2 mm (Anzalone et al., 2013) Some of the volumetric acquisitions, such as spoiled gradient echo and magnetization-prepared rapid gradient echo

(MP-RAGE), may provide finer detail and enhance the detection of smaller lesions, although the signal-to-noise ratio may be slightly less than for traditional spin-echo sequences. Volumetric fast spin echo (SPACE) has been shown to outperform volumetric gradient echo (MP-RAGE) imaging at 3 T (Reichert et al., 2013), and subsequent confirmatory results also have been reported (Kwak et al., 2015). A recent meta-analysis also concluded that three-dimensional spin echo is better than gradient echo imaging, particularly for the detection of small metastases (Suh et al., 2016), but these spin echo sequences may be less widely available than commonly available gradient echo sequences such as spoiled gradient echo and MP-RAGE.

Although contrast is typically used in conjunction with T1W images, contrast can impact other MR acquisitions as well. For instance, postcontrast FLAIR images may improve the detection of leptomeningeal metastases (Singh et al., 2000; Ercan et al., 2004; Hatzoglou et al., 2016). But in most cases volumetric contrast-enhanced sequences provide better sensitivity for leptomeningeal disease than two-dimensional T1-weighted or FLAIR images (Gil et al., 2016).

Sequences other than T1 and FLAIR also can be selected that are sensitive to specific characteristic of metastases. For instance, gradient echo and other susceptibility-weighted images (SWI) are highly sensitive to the local perturbation in magnetic field that is associated with the deposition of hemosiderin and other blood breakdown products. Thus these techniques may improve detection of hemorrhagic metastases, particularly melanoma (Gaviani et al., 2006). SWI has been found to increase the sensitivity for the detection of small hemorrhagic metastases, although very small lesions (< 1 mm) are rarely SWI-positive (Franceschi et al., 2016).

Although currently MRI scans are interpreted by radiologists and other practitioners unaided by machine learning, methods for the automated detection of metastases and other brain lesions are being developed. The addition of these algorithms to human interpretation could potentially lead to greater sensitivity and improved accuracy of intracranial metastases characterization, based both on standard postcontrast exams as well as advanced physiologic imaging such as perfusion-related acquisitions (Ambrosini et al., 2010; Yang et al., 2013; Szwarc et al., 2015).

PRINCIPLES UNDERLYING ADVANCED IMAGING TECHNIQUES (TABLE 7.1)

Perfusion imaging

There are multiple approaches to acquiring MR data that can generate metrics related to tumor perfusion. The most commonly used methods are dynamic susceptibility contrast (DSC), dynamic contrast-enhanced (DCE), and arterial spin labeling (ASL) techniques. Although many different kinds of measurements can be derived from any of these approaches, some have been demonstrated to be particularly useful. These metrics include cerebral blood volume (CBV), which is a measure of the amount of blood within a defined volume of tissue (typically 100 g), and correlates with tumor vascularity. This is acquired with a bolus tracking method coupled with a susceptibility-sensitive (T2*-weighted) sequence (DSC). The passage of intravenous contrast through the tissue reduces the T2*

signal intensity, and this is proportional to the blood flow. DSC can be acquired rapidly, usually in approximately 2 minutes. Potential limitations are susceptibility artifact from blood products, air, adjacent bone, or implanted devices such as shunts or metallic craniotomy plates. Thus the use of DSC in postoperative patients can be particularly challenging.

Typically CBV is expressed as a ratio of that within the tissue of interest to the contralateral brain (mirror site) or contralateral normal-appearing white matter. Unfortunately, CBV measurements are impacted by a variety of factors, including scanner hardware and protocol specifics. These include the use of a “preload” contrast dose to minimize T1 leakage effects that occur in areas of blood–brain barrier disruption, leakage correction on postprocessing software, flip angle, and region of interest (ROI) selection. Currently efforts are underway to standardize DSC image acquisition, especially in the setting of multicenter drug trials for glioblastoma and other primary brain tumors. However, even with better standardization there likely will be substantial interinstitutional and even intrainstitutional variation in CBV measurements due to hard-to-control variables in imaging acquisition. This degrades the ability to set optimal thresholds for tumor recurrence and other clinical applications (Boxerman et al., 2016).

Ktrans, a transfer contrast coefficient, is another commonly used perfusion-based metric. Ktrans is derived from DCE imaging and is related to the leakiness of blood vessels. DCE is acquired by measuring changes in signal intensity associated with passage of contrast using dynamic T1-weighted sequences. The signal change is affected by both intra- and extravascular contrast, which is the basis for estimating contrast leakage. DCE has the advantage of being less sensitive to susceptibility artifacts than DSC, but overall appears to be more challenging to acquire (Griffith and Jain, 2016).

In distinction to DSC and DCE imaging, ASL is acquired without the use of GBCA. Instead ASL uses labeling of blood water protons to provide an endogenous tracer. ASL techniques are typically used to generate relative and quantitative measures of cerebral blood flow (CBF). CBF is typically defined as the amount of blood that passes through the tissue of interest per unit of time (typically expressed as mL/100 g tissue/minute). Mean transit time of blood through tissue also can be acquired (Grade et al., 2015).

Diffusion-weighted imaging

DWI is a collection of acquisition sequences that are sensitive to the motion of water molecules. All water molecules in environments with temperature above absolute zero will undergo Brownian or thermal motion, which in pure water will be random and isometric (equal in all directions). A surrogate for this motion (termed the apparent diffusion coefficient (ADC)) can be acquired by MRI techniques. Areas of abnormality that are reduced in diffusion are bright on DWI. The b value of the image represents the diffusion weighting. Multiple images with varying b values are acquired to generate the ADC map. On the ADC map, areas of restricted water diffusion are of dark or low signal intensity. In general, vasogenic edema increases the diffusivity of water, resulting in increased ADC values. Conversely a variety of biophysical properties of tissue can result in decreased or restricted diffusion. These include cytotoxic edema (cell swelling), increased cellularity, and

fluid collections that contain high levels of proteinaceous or other molecular species that interact with water molecules and limit their ability to move freely. Thus, for instance, abscesses typically have restricted diffusion and are of low signal intensity on ADC images. It is important to note that various processes within a single tissue can impact water diffusivity in opposed directions, yielding no or little net change in DWI signal characteristics. Thus a combination of vasogenic and cytotoxic edema found in subacute to chronic infarct may show normal ADC values even though the tissue state is abnormal (Baliyan et al., 2016).

Diffusion tensor imaging (DTI)

In addition to isometric diffusion, which proceeds equally in all directions, there also is diffusion that is directional, i.e., preferential in a given direction. DTI is an MR technique that can be used to detect the directed motion of water molecules. This is typically acquired with a larger number of diffusion acquisitions, each sensitive to a specific direction of diffusion. Metrics associated with DTI are fractional anisotropy (FA) and mean diffusivity (MD). FAvalues range from 0 (no directionality of diffusion) to 1 (complete unidirectional diffusion). MD is a measure of average molecular motion that is independent of any tissue-based directionality. Diffusion in the brain is greatly affected by brain structure, as the directionality of diffusion is high longitudinal to white-matter tracts, but low perpendicular to them (Baliyan et al., 2016).

MR spectroscopy (MRS)

MR proton spectroscopy can be used to measure concentrations of metabolites in tissue. A large number of metabolites can be measured within a volume of interest (voxel), although low concentration of many metabolites makes repeatability and accuracy a challenge. The more abundant metabolites and ones that are commonly measured include N-acetyl aspartate (NAA), a marker of neuronal integrity, choline (Cho), which is associated with membrane turnover and can correlate with cell density in glioma, and creatine (Cr), which is a set of closely related molecules that are impacted by energy storage and often used as an internal control. Thus the concentration of other metabolites may not be measured in absolute values, but rather normalize against Cr levels. Lipids, lactate, amino acids, and myoinositol often are also typically detected on MRS (Brandao and Castillo, 2016; Rapalino and Ratai, 2016).

Positron emission tomography

PET is an imaging modality that can complement MRI or CT, providing information on metabolism of brain metastases and other abnormalities (Jones et al., 2012). A variety of PET tracers have been developed, often incorporating the positron emitter ^{18}F due to its longer half-life (110 minutes) compared to other radioactive species such as ^{11}C (half-life 20 minutes). By far the most commonly used tracer in clinical applications is FDG. FDG is a glucose analog that is taken up by cellular glucose transporters, and then undergoes intracellular phosphorylation, trapping the molecule in the cell and inhibiting its further metabolism. This results in increased uptake in cells that are metabolically active, as evidenced by increased glucose consumption.

There are several limitations in using FDG tracers in the brain, probably the most fundamental of which is the high background activity present in the cortex and basal ganglia (due to intrinsic high glucose consumption of these structures). This high background activity can substantially degrade signal-to-noise ratio when FDG is employed (Juhasz et al., 2014). PET, in general, also is hampered by low resolution (around 5 mm, compared to 2 mm or less for MRI) based on technical factors, including the minimum number of positron electron annihilation events needed to meet the threshold for detection. These limitations adversely affect the ability of PET to detect small lesions. Thus the sensitivity and specificity of FDG PET for the detection of brain metastases are considerably lower than MRI (Rohren et al., 2003; Ohno et al., 2007; Krüger et al., 2010).

Non-FDG PET

In addition to FDG PET, other tracers, most importantly those that reflect amino acid metabolism, are used to characterize primary and metastatic brain tumors. Amino acid PET tracers are not reliant on blood–brain barrier breakdown for uptake, as they undergo active transport by the L-amino acid transporter type 1 system, and thus can add value to contrast-enhanced MRI. Amino acid tracers have notably lower brain background activity than FDG, which is a substantial advantage. In gliomas, amino acid uptake correlates with a variety of malignant processes, including cell proliferation and neoangiogenesis. For glioma imaging the use of two PET tracers has become widespread: O-(2-[^{18}F]fluoroethyl)-L-tyrosine (FET) and 3,4-dihydroxy-6-[^{18}F]-fluoro-L-phenylalanine (FDOPA) (Galldiks et al., 2015). ^{11}C-MET is less widely used due to its shorter half-life of 20 minutes, requiring on-site cyclotron for its generation (Juhasz et al., 2014). Amino acid PET is also now being more widely investigated for potential applications in brain metastatic disease.

DIFFERENTIATING METASTASES FROM SIMILAR-APPEARING MASSES

Intracranial metastases typically enhance, as they lack a blood–brain barrier. The differential diagnosis for enhancing brain lesions is broad, but can be narrowed by the patient's presentation and laboratory data. Enhancing brain lesions are typically categorized into single versus multiple, and ring- versus solidly enhancing, to facilitate generation of a list of potential diagnoses. Although brain metastases are usually multiple, single brain metastases are not uncommon, with an incidence of 25–45% (Patchell et al., 1990; Schwartz et al., 2006), and can be found in 15% of patients who show no evidence of a primary lesion following additional workup (Nussbaum et al., 1996). Many common malignancies have a propensity for singular brain metastases, including breast, colon, renal cell, and thyroid cancers, whereas lung cancer and melanoma are more likely to generate multiple brain tumors (Barajas and Cha, 2012).

Nodular solid enhancement, either singular or multiple, can be found in a variety of pathologies, including metastatic disease, lymphoma, sarcoid, vasculitides, including Behçet disease, demyelinating disorders, and infections, including tuberculosis (tuberculomas), toxoplasmosis, and fungal disease (Fig. 7.3) (Packer and Schiff, 2012). For ring-enhancing lesions the most common etiologies are high-grade glioma (40%), metastases (30%), abscess (8%), and demyelinating disease (6%) (Schwartz et al., 2006). Necrotic primary central

nervous system lymphoma can be ring-enhancing and centrally necrotic, but this is rare (6% in one study) and typically associated with immunocompromised patients (Fig. 7.3E) (Malikova et al., 2016). Metastases are most often cortical or subcortical due to hematogenous spread and often start as smaller, solidly enhancing lesions, before becoming ring-enhancing secondary to necrosis either from outstripping available blood supply or following treatment such as chemotherapy or irradiation (Smirniotopoulos et al., 2007).

Diagnosis of a single ring-enhancing brain lesion remains difficult and is an active area of imaging research. In particular, differentiating single metastases from glioblastoma remains a top diagnostic challenge in everyday clinical practice due to the high incidence of these lesions and their potential to have essentially identical appearance on standard MRI. This can lead to a misclassification rate of up to 40% (Devos et al., 2004; Georgiadis et al., 2008). Advanced imaging, including diffusion and perfusion sequences, has been extensively investigated as a means of decreasing diagnostic uncertainty in these cases, particularly in patients with no known primary tumor who present with a solitary enhancing lesion (Fig. 7.4).

Before trying to distinguish between the possibility of glioblastoma and metastases, often a good first step is to assess the possibility that the lesion could represent abscess, demyelinating disease, or lymphoma, since even standard MRI may help identify these entities. For instance, open-ring or “C-shaped” enhancement, restricted diffusion, and relatively little mass effect are associated with demyelinating disease (Fig. 7.3D) (Masdeu et al., 2000; Siri et al., 2015; Abdoli et al., 2016). Primary central nervous system lymphoma is typically solidly enhancing in immunocompetent patients, is superficial or periventricular, and also shows decreased diffusion due to its high cellularity (Yamasaki et al., 2005; Lin et al., 2017). Thus careful assessment of standard imaging, including the ADC map, usually prevents tumefactive multiple sclerosis or lymphoma from being confused with metastatic disease. In addition to standard imaging, other MR applications may be helpful for resolving diagnostic uncertainty. For instance, MRS findings of increased lipids and lactate in a solid lesion can be indicative of lymphoma (Smirniotopoulos et al., 2007). Lymphoma typically does not have vessels detectable by susceptibility weighting, in contrast to glioblastoma and metastases (Ding et al., 2014).

DWI is extremely helpful in identifying pyogenic abscesses, which otherwise may mimic glioblastoma or metastasis. Typically pyogenic abscesses show diffusion restriction, whereas diffusion restriction is rarely found in metastases or glioblastoma (Smirniotopoulos et al., 2007). The identification of diffusion restriction within a ring-enhancing lesion has to be interpreted with caution, however, as occasionally glioblastoma and metastases have been known to have restricted diffusion (Hartmann et al., 2001; Hakyemez et al., 2005; Reddy et al., 2006). Conversely, unrestricted diffusion has been reported in 4/97 (4%) abscesses (Reddy et al., 2006). Nevertheless, in a meta-analysis of 11 studies, DWI was shown to be highly effective at differentiating abscess from other intracranial, ring-enhancing cystic mass lesions with an accuracy of >95% (Xu et al., 2014). Further, FA of the enhancing rim (derived from DTI) appears to improve the ability to discriminate abscesses from both glioblastoma and metastasis, yielding 100% accuracy in a study of 15 abscesses, 15 glioblastomas, and 26 cystic metastases (Toh et al., 2011).

Thus diffusion imaging can greatly aid in the identification of lymphoma, abscesses, and, to a lesser extent, lymphoma. Diffusion imaging has also been applied to the more challenging difficulty of discriminating solitary brain metastasis from glioblastoma. The most direct approach is to measure tumor ADC, as this can be done easily on most Picture Archiving and Communication Systems (PACS). Unfortunately, while tumoral ADC helps differentiate some tumor types, it does not appear to distinguish glioblastoma from metastases (Bulakbasi et al., 2004; Yamasaki et al., 2005).

Another approach is to measure diffusion in peritumoral regions rather than within the tumor itself. This is predicated on the hypothesis that peritumoral regions of high T2 signal intensity represent edema only in metastases, whereas these regions contain both edema and infiltrative tumor cells in glioma. This infiltration of peritumoral regions by tumor cells in glioma results in diminished ADC values. Supporting this hypothesis, peritumoral ADC is lower in both anaplastic astrocytoma and glioblastoma compared to metastases (Pavlisa et al., 2009; Han et al., 2014). High b value diffusion imaging (3000 compared to the standard 1000) may slightly improve this approach, as one study found that using a minimum ADC value, the area under the curve (AUC) was 0.92 for b = 3000 compared to 0.89 for b = 1000 (Han et al., 2014). ADC in normal-appearing white matter, beyond the area of T2 signal abnormality, has also been analyzed. Although there was a difference in minimum ADC values in normal-appearing white matter between patients with glioblastoma and metastases, the sensitivity and specificity for differentiating the two were disappointing (both approximately 70%), limiting the clinical utility of this approach (Miquelini et al., 2016).

In addition to standard diffusion imaging, DTI-derived metrics have been applied to this diagnostic challenge. Lu and colleagues (2003) examined DTI in high-grade gliomas (HGG: $n = 12$) and metastases ($n = 12$). They found that peritumoral MD of metastases was higher than HGG. There was no difference in FA. In a much larger study (165 glioblastoma, 129 metastases), there was no difference in peritumoral FA, but there was a difference in FA within the contrast-enhancing lesion, which was significantly higher in glioblastoma than metastases (0.33 and 0.23 respectively; $p < 0.0001$) (Bette et al., 2016b).

Like Lu et al. (2003), Byrnes and colleagues (2011) found that metastases have higher peritumoral MD than glioblastoma. However, unlike both Lu et al. and Bette et al., they also report a difference in FA in peritumoral edema, which was higher in metastases than glioblastoma. Combining these metrics the authors correctly identify 24/28 tumors as either glioblastoma or metastasis (Byrnes et al., 2011). Thus if the differential diagnosis for a ring-enhancing lesion can be narrowed to HGG and metastasis, investigation of the peritumoral region with diffusion imaging may help successfully identify the underlying lesion. As some disparate findings for the optimal diffusion-based metrics have been reported, further validation is necessary. Another caveat is that the underlying theory, namely that peritumoral T2 signal abnormality is secondary to pure edema for metastases, may not be entirely accurate. As with glioma, parenchymal invasion may also be a feature of metastatic disease. In fact, in one study 18 out of 57 (32%) brain metastases showed a diffuse infiltrative pattern. Invasion was present up to 450 μm from the border of the metastatic tumor and was not dependent on the primary tumor type (Berghoff et al., 2013a). Thus use of DTI-based

metrics in peritumoral edema may never achieve 100% accuracy in distinguishing metastases and glioma.

In addition to diffusion-based techniques, MR perfusion imaging has focused on the region of peritumoral T2 signal abnormality to detect changes that may differentiate metastases from mimics. For instance, DSC perfusion has been used to distinguish abscess from glioblastoma and cystic metastases (Toh et al., 2014). Toh et al. measured CBV in the enhancing rim of abscesses, glioblastoma, and metastases. They found that abscesses had lower CBV (1.97 ± 1.01) than glioblastoma (4.39 ± 2.33) or metastases (2.97 ± 0.78). They report an AUC of 0.82 for differentiating abscesses from glioblastoma and metastases combined.

Looking specifically at the ability to distinguish abscess from neoplasm, Floriano and colleagues (2013) examined 100 consecutive patients with DSC-based relative CBV (rCBV). Neoplasms had higher rCBV than infection (4.3 ± 2.11 vs. 0.63 ± 0.49). Using a cutoff of <1.3, infectious lesions were identified with a sensitivity of 98% and specificity of 93%. However, the vast majority of the infectious lesions in this study were toxoplasmosis (38/46, 83%), so this finding may be specific to that infection. Interestingly, rCBV did not distinguish glioblastoma from metastases (Floriano et al., 2013).

Server and colleagues (2011) investigated DSC-based metrics in tumor and peritumoral regions in order to distinguish glioblastoma ($n = 40$) from metastasis ($n = 21$). rCBV of the peritumoral region was better than that from the tumor itself in distinguishing the two, with receiver operating characteristic AUC of 0.98, similar to a prior study where the AUC was 0.96 (Bulakbasi et al., 2005). Similarly, in a series of glioblastoma ($n = 29$) and metastases ($n = 23$), peritumoral rCBV discriminated metastases from glioblastoma with a sensitivity of 96% and specificity of 64%. The authors conclude that metastasis is unlikely if peritumoral rCBV is > 1 on any slice depicting the tumor (Blasel et al., 2010).

More recently, in a large study qualitative and quantitative ASL-based perfusion metrics were analyzed in a population of 128 consecutive patients who had either glioblastoma or metastasis at surgery. Glioblastoma-normalized CBF values were higher both in the enhancing tumors and in the peritumoral area of T2 signal change than those of metastatic tumors. Peritumoral CBF data provided the best discrimination between glioblastoma and metastases with an AUC of 0.54 ($p < 0.001$) (Sunwoo et al., 2016).

A similar study (Lin et al., 2016) reported analysis of the gradient of CBF from areas immediately adjacent to the tumor to normal-appearing white matter, using ASL data. A total of 52 consecutive patients with either glioblastoma or solitary brain metastasis were assessed. Subtracting the distant CBF values from the tumor-adjacent areas resulted in 93% sensitivity and 100% specificity for differentiating glioblastoma from metastases. For glioblastoma, CBF diminished in the area of peritumoral T2 signal change as ROIs were placed farther from the enhancing tumor margin. Conversely, for metastases, CBF appeared fairly constant throughout the area of peritumoral T2 signal change, irrespective of the distant from the enhancing lesion. As with diffusion, this difference in perfusion characteristic may be due to the more infiltrative nature of glioma compared to metastases.

Another interesting, although preliminary, report based on qualitative rather than quantitative data found that ASL-generated CBF maps show a rim of high peritumoral signal in glioblastoma and lymphoma but not metastases. If there was ASL signal abnormality extending beyond the area of contrast enhancement, than the lesion was unlikely to be metastatic disease (Abe et al., 2015), providing a rapid and easy qualitative method to distinguish the two diseases. Thus a number of qualitative and quantitative perfusion-based approaches have been developed to differentiate metastases from glioblastoma, but it remains unclear which is the most accurate and reproducible across institutions.

Spectroscopy has been investigated as a means of differentiating metastases from HGG and other mimics, with mixed results. In general, while some pathologies can potentially be distinguished by MRS, the spectra of glioblastoma and metastases tend to be highly overlapping. This is not unexpected, as both often contain central necrotic regions that exhibit lower NAA due to neuronal destruction, but increased lipid and lactate peaks, a nonspecific finding associated with necrosis. However, there may be some differences in the spectra between these tumor types. For instance, the concentration of lipids and macromolecules may be higher in metastases than glioblastoma. Measurements based on this approach discriminated the two entities with an accuracy of approximately 80% in one report (Crisi et al., 2013).

More commonly, MRS has been used to measure the Cho/Cr, NAA/Cr, and Cho/NAA levels in both tumoral and peritumoral areas. As with perfusion data, interrogation of peritumoral regions may be particularly informative. For instance, Chiang and colleagues (2004) report a higher peritumoral Cho/Cr of 1.3 ± 0.45 for HGG ($n = 14$) vs. 0.29 ± 0.51 for metastases ($n = 12$). In a much larger study of 65 tumors, peritumoral Cho/Cr also was found to be an excellent discriminator (94% AUC) when comparing either glioblastoma alone, or both glioblastoma and anaplastic astrocytoma, to metastases (Server et al., 2010). The authors also found that metabolite measurement from peritumoral areas was better than that from tumors, similar to other studies (Tsougos et al., 2012; Weber et al., 2006). Some important caveats for this technique remain. To date these studies are mostly retrospective and include only HGG and metastases. The inclusion of other pathologies could negatively impact the accuracy of these MRS-based biomarkers. Additionally, up to 30% of glioblastoma do not have evidence of abnormal peritumoral spectra (Tsougos et al., 2012), which would make the ability to discriminate these glioblastoma from metastases based on MRS alone unlikely to be sufficiently accurate for clinical applications.

PET also has been used as a tool for narrowing the differential diagnosis of brain lesions. However, neither FDG nor amino acid PET appears to distinguish metastases from common mimics such as glioblastoma. Although FET uptake may be higher in HGG than low-grade glioma (Rapp et al., 2013), values for glioblastoma, metastases, and inflammatory lesions such as multiple sclerosis can be overlapping, and even epileptogenic activity can result in abnormal FET uptake (Hutterer et al., 2013,2017). For instance, in a large study ($n = 393$ patients) using FET, normalized standardized uptake value of HGG and nonglial tumors were not dissimilar (1.99 ± 0.74 and 2.09 ± 0.62, median ± SD, respectively) (Hutterer et al., 2013). Another limitation is that the sensitivity of FET PET for small metastases (< 1.0 cm) is low (Unterrainer et al., 2017).

The search for new PET tracers that may overcome some of these limitations is ongoing. For instance, Kamson and colleagues (2013) used a relatively new PET tracer that is a tryptophan analogue (11C-alphamethyl-L-tryptophan), and compared enhancing lesions that were either glioblastoma ($n = 19$) or metastases ($n = 31$). Based on this method they were able to differentiate glioblastoma from metastases (glioblastoma had higher uptake) with 74% accuracy. When analyzing only the subset of ring-enhancing lesions, diagnostic accuracy improved to 91%. Further refinements of available PET tracers may continue to yield improvements in diagnostic accuracy.

While many studies focus on a single biomarker for diagnostic challenges, some studies have employed a multiparametric approach that combines various imaging classifiers in an effort to maximize the diagnostic accuracy of imaging. A small study of 23 patients (13 glioblastoma, 10 metastases) used DSC, DCE perfusion, and DTI. Once again, interrogation of the peritumoral region was most helpful in discriminating metastases and glioblastoma, using a combination of rCBV, FA, and MD. This led to an AUC of 0.98 (Bauer et al., 2015). Others have used a multiparametric approach based on both perfusion and MRS. Sparacia and colleagues (2016b) analyzed maximal rCBV and Cho/Cr ratios in the peritumoral nonenhancing areas from 28 patients (10 low-grade glioma, 8 HGG, 10 metastases). Gliomas, regardless of grade, had rCBV > 1.2, whereas only 1 of 10 metastases did (yielding a sensitivity of 100%, specificity of 90%). Additionally, MRS metrics were significantly different between glioma and metastases. Similarly, peritumoral rCBV combined with Cho/NAA can discriminate glioblastoma from metastases with an AUC of 0.85 for rCBV and 0.87 for Cho/NAA (Tsougos et al., 2012).

Two recent meta-analyses have been performed examining the ability of advanced MRI to differentiate HGG from metastases. Importantly, the first analysis was based only on papers analyzing the peritumoral region (Liang et al., 2014), whereas the more recent analysis was performed only on papers analyzing the enhancing tumor region (Usinskiene et al., 2016). Thus the recent meta-analysis based on 83 articles published since 2000 analyzing the contrast-enhancing region found that advanced imaging, including perfusion and diffusion imaging (rCBV, normalized ADC, Cho/Cr, Cho/NAA), although informative in separating high- from low-grade glioma, cannot reliably differentiate HGG from metastases (Usinskiene et al., 2016). Conversely, the meta-analysis that focused specifically on rCBV in the peritumoral region did find a fairly good ability to discriminate between glioblastoma and metastases, with a sensitivity of 82%, specificity of 96%, and a diagnostic odds ratio of 90 (Liang et al., 2014).

Machine-learning paradigms provide a method to incorporate much more of the available MR data from standard and advanced imaging protocols into models that may improve diagnostic accuracy. For instance, Tsolaki and colleagues (2013) examined NAA/Cr, Cho/Cr, lipid + lactate/Cr and rCBV from 35 glioblastoma and 14 metastases. While the radiologist diagnosis was accurate in approximately 75% of cases, a support vector machine-learning approach made a correct diagnosis in 97% of tumors. Similar papers report diagnostic accuracy in the 75–86% range (Vellido et al., 2012; Svolos et al., 2013), indicating that automated or semiautomated methods may be as accurate as, or more accurate than, standard radiologic interpretation. Another interesting semiautomated

approach is to use DTI data to assess tumor shape and “curveness,” as glioblastomas tend to be more irregularly shaped than metastases. Using such a morphologic analysis, a 96% diagnostic accuracy in discriminating glioblastoma from metastases was achieved (Yang et al., 2015). The addition of other classifiers, such as the ratio of edema to tumor, may further improve machine-learning approaches (Zhou et al., 2016).

To summarize, for distinguishing brain metastases (particularly single ring-enhancing lesions) from common mimics in clinical practice, DWI may help narrow the likely differential diagnosis to glioblastoma and metastases. Peritumoral NAA/Cr, Cho/Cr, Cho/NAA ratios, and rCBV seem to help differentiate these two entities. The utility of diffusion-based metrics, including ADC or FA, remains more controversial. Multimodalitybased approaches potentially in combination with machine-learning methods may end up being the most comprehensive and accurate paradigm to diagnose metastases, but validation and standardization remain a challenge.

DETERMINING UNDERLYING PRIMARY TUMOR

As the underlying primary lesion in brain metastatic disease is unknown in 10–15% of cases (Polyzoidis et al., 2005), it would be helpful if imaging features of brain metastases could help identify the primary malignancy, or at least narrow the differential diagnosis.

Patterns in the location of brain metastases may vary between primary tumors. For instance, nonsmall cell lung carcinoma tends to favor the parietal occipital lobes, whereas breast cancer metastases may occur more often in the cerebellum (Quattrocchi et al., 2012). Esophageal metastases typically have a cystic appearance with a small surrounding edema zone of less than 2 cm (Feng et al., 2014). Additionally, even subtypes of common tumors may have varying appearances when metastasized to the brain: triple-negative breast cancer metastases tend to be cystic necrotic (have a thin wall with central necrosis), compared to other breast cancer subtypes (Yeh et al., 2014).

MRS has been used to try to distinguish nonsmall cell lung carcinoma from both melanoma and breast metastases, based on Cho/Cr ratio (Huang et al., 2010). A Cho/Cr ratio of < 2.0 is seen in 38% of lung cancer metastases, 24% of breast cancer metastases, but in 0% of melanoma metastases, suggesting this method could help exclude the possibility of melanoma. High lipid content measured by MRS is associated with colorectal carcinoma (Chernov et al., 2006), although sensitivity of 88% and specificity of 64% limit clinical utility.

SWI is extremely sensitive to blood products. The majority of both breast (56%) and melanoma (77%) metastases have abnormal SWI signal; that is, they are SWI+. Therefore a binary classification system (SWI+ vs. SWI−) does not distinguish between the two (Franceschi et al., 2016). However, when the amount of SWI signal abnormality within a metastatic lesion is quantified, melanoma can be distinguished from both breast and bronchial cancer with excellent accuracy (receiver operating characteristic 0.96 and 0.81 respectively), as melanoma metastases tend to have a larger percentage of voxels that show abnormal SWI hypointentsity (Radbruch et al., 2012).

Diffusion imaging has also been applied to this clinical dilemma of identifying the primary tumor, but with limited success (Meyer et al., 2015). In one study ADC values of brain metastases in 159 patients were analyzed. Nonsmall cell lung carcinoma had slightly lower mean ADC values than breast or melanoma metastases but the difference was not statistically significant. One limitation was that some tumors could not be evaluated because of hemorrhage. Similarly, others have found no correlation between ADC values and primary tumor histopathology (Duygulu et al., 2010).

Lastly, PET ligands that may have specificity for primary tumor types, such as prostate carcinoma (Chakraborty et al., 2015) and neuroendocrine tumors (Kunikowska et al., 2014), also are being investigated, but are in very early stages of development.

Thus, current imaging paradigms for brain metastases appear to have limited ability to identify the underlying primary tumor type.

TREATMENT PLANNING

MRI plays a critical role in treatment planning for brain metastases, helping to identify the number, size, and location of lesions, leading to improved surgical and radiation-based therapies. FET PET may add value to standard MRI for optimization of treatment planning, as FET PET can show areas of potential tumor that in some cases extend beyond the contrast-enhancing region on MRI (Gempt et al., 2015).

Studies have also investigated the use ofMET PET for treatment planning, comparing MET PET to MRI in patients with recurrent disease following gamma knife SRS. In one such study the authors found that, even though the irradiation volumes were smaller when based on MET PET imaging compared to MRI alone, the survival times were longer, suggesting that MET PET more effectively targeted lesions than MRI alone (Momose et al., 2014). Similar results may be expected with FET PET, as FET and MET uptake appear comparable in pretreated brain metastases (Grosu et al., 2011).

Diffusion imaging for treatment planning may also help reduce the risk of recurrence. The use of ADC data in addition to postcontrast T1 images results in unchanged gross tumor volumes but modulates target shapes. In a study by Zakaria et al. (2017) the diffusion-based treatment area was found to cover a larger volume of subsequent tumor recurrence, and thus may provide patient benefit, pending survival analysis. As invasion could be underrecognized phenomena of metastasis, the ability to noninvasively identify areas of infiltrative tumor spread could also help optimize treatment plans. This can potentially be achieved with analysis of ADC data.

In another study, fusion of ADC maps from intraoperative scans to anatomic imaging appeared to help delineate areas of tumor border zone where parenchymal invasion was occurring and better define tumor margins (Zakaria and Jenkinson, 2014).

TYPICAL TREATMENT RESPONSE IMAGING CHANGES

As SRS plays a major role in the treatment of brain metastases, it is important to be aware of the changes that can be induced by radiation-based treatment paradigms. Response to SRS and other treatments is typically determined with serial MRI (Sparacia et al., 2016a). After radiosurgery 3-month imaging follow-up has been recommended by the American College of Radiology (Patel et al., 2012). In general, following irradiation, metastases may demonstrate increased edema, central T2 hypointensity, and blurred enhancement. They may also increase slightly in size as a response to treatment, which does not indicate progressive tumor. In a review of MRI changes in 500 treated brain metastases, approximately one-third of lesions showed a transient increase in volume that typically began at approximately 6 weeks posttreatment and which could last, in some cases, beyond 15 months (Patel et al., 2011). Following successful treatment metastases will shrink, edema will abate, but focal abnormal signal intensity may never completely resolve. Formalized classification of treatment response has recently been proposed by multidisciplinary groups. This includes specifications for parenchymal (Lin et al., 2015) and leptomeningeal disease (Chamberlain et al., 2017).

EARLY RESPONSE MARKERS

ADC may be an early response marker for SRS or whole-brain radiotherapy. For instance, low ADC of enhancing regions has been correlated with responders at both 1 week and 1 month after treatment (Jakubovic et al., 2016). Conversely, others have found that increased ADC values predict improved response (Lee et al., 2014; Ruiz-Espana et al., 2015). Changes in ADC are dynamic so that the time at which change is measured may be crucial. Effective therapy may initially induce cytotoxic edema (which would lower ADC), but subsequently induce cell death and necrosis and also edema (which would increase ADC). Clearly the time course of the underlying pathophysiology of irradiated brain metastases needs to be determined in greater detail to improve interpretation of ADC-based metrics.

Perfusion data of irradiated metastases have been analyzed to help identify tumor response, again with somewhat conflicting results. In one study, lower Ktrans and lower relative CBF (rCBF) at 1 week after treatment correlated with responders, whereas higher rCBF and rCBV at 4 weeks were associated with therapy benefit (Jakubovic et al., 2014). Another study also analyzed Ktrans data and found that even a small increase in Ktrans at 4–8 weeks after SRS was associated with tumor progression (Almeida-Freitas et al., 2014), similar to a prior analysis that found that increased CBV at 6 and 12 weeks is associated with worse outcome (Fig. 7.5) (Essig et al., 2003). Thus, as for ADC, given the dynamic changes associated with treatment effect, the time point for measuring perfusion appears crucial. Specifically, responders may initially (at 1 week) have lower perfusion, but the direction of perfusion changes that correlates with response when measured at 1 month is unclear. At later time points increased perfUsion is likely indicative of a poor response. It may be that successful SRS decreases perfusion initially in most tumors, but nonresponders then rebound quickly, increasing their perfusion.

Comparison of data from different studies is also challenging due to the variety of perfusion-based metrics that are analyzed. Additional studies that standardize some of the acquisition variables and focus on the time course of changes in rCBV (often thought of as the most robust and widely used perfusion metric) will potentially help resolve these conflicting data.

In preliminary studies PET scans have been used to identify effects of treatment that may not be apparent on MRI. For instance, FDG PET activity diminishes in some patients with HER2 + breast cancer metastases that are successfully treated (Shankar et al., 2006). Specific PET tracers such as the monoclonal antibody ^{89}Zrtrastuzumab are able to detect brain metastases in HER2 + breast cancer with a good uptake-to-background ratio (Dijkers et al., 2010). For breast cancer brain metastases treated with paclitaxel covalently linked to angiopep-2, changes in FLT PET correlated with MRI findings in a pilot study of 10 patients after a single treatment cycle and appeared to correlate with outcome (O'Sullivan et al., 2016). Extracranially, changes at 3 weeks in HER2+ patients correlate with tumor response at 8 weeks as measured by CT; this is not true for FDG PET (Gaykema et al., 2013). Thus ^{89}Zrtrastuzumab PET may outperform FDG PET as an early response marker, although studies specifically assessing brain metastases have yet to be performed.

Imaging-based early response markers for brain metastases have been an active area of investigation and clearly have significant potential to improve patient care. To date, it appears that advanced imaging metrics, whether based on MRI or PET, have not been sufficiently developed and validated to allow their clinical use.

CAVEATS TO INTERPRETING POSTTREATMENT IMAGING CHANGES

Radiation necrosis

Increase in size of brain metastases is not always indicative of tumor progression. As with other tumors, such as glioma, radiation effects can yield imaging changes that can be misinterpreted as tumor progression. More acutely (within 6 months), these changes are generally termed pseudoprogression, whereas after 6 months, the effect may be the result of classic radiation necrosis, although there is some overlap between the two phenomena. Regardless, they are both characterized by increased enhancement mimicking tumor growth. Thus the ability to identify radiation change in post-SRS-treated metastases has been the focus of intense investigation. To date, rCBV and amino acid PET show the most promise in differentiating the two processes.

For perfusion imaging, visual inspection of the rCBV map alone (Fig. 7.6) can differentiate tumor recurrence following SRS from radiation necrosis with a sensitivity of 70% and specificity of 93%. Quantitative analysis, using an ROI cutoff of 2.0 (lesion compared to white matter), increases accuracy (Hoefnagels et al., 2009). Similarly, others have found excellent sensitivity and specificity for quantitative CBV-based methods (100% and 95% using a cutoff of 2.1 ratio of lesion to normal brain) (Mitsuya et al., 2010). In addition to calculating rCBV, washout curves from DSC perfusion images have diagnostic value as radiation necrosis has more recovery towards baseline perfusion values than do metastases. Thus the signal recovery has 96% sensitivity and 100% specificity in identifying radiation necrosis. This is better than using an rCBV cutoff of 1.52, which yields a sensitivity of 91%

and specificity of 73% (Barajas et al., 2009). Similarly, measuring the time course of contrast enhancement may help identify radiation necrosis. From 2 to 15 minutes after contrast administration both radiation necrosis and metastasis show increased enhancement; however, by 55 minutes enhancement continues to increase in radiation necrosis but diminishes in metastatic disease. Thus metastasis seem to have a quicker washout than radiation necrosis (Wagner et al., 2016). A prospective study using DCE perfusion data found that a plasma–volume ratio ≥ 2.6 identified progression versus radiation treatment effect with sensitivity of 91% and specificity of 80% (Hatzoglou et al., 2015). Although perfusion MRI-based rCBV appears more accurate than MRS (Huang et al., 2011), a meta-analysis has shown that both rCBV and Cho/Cr help differentiate true progression from radiation necrosis (Chuang et al., 2016).

Exploratory MRI techniques such as chemical exchange saturation transfer provide new methods of generating tumor contrast and can be used to interrogate variables such as pH, acidity, lactate levels, and other aspects of cellular metabolism and microenvironment (Harris et al., 2015, 2016; Longo et al., 2016). Chemical exchange saturation transfer has been used to distinguish recurrence from radiation necrosis in a pilot prospective study of 16 patients with brain metastases treated with SRS (Mehrabian et al., 2017). There was little overlap between recurrence and radiation necrosis, suggesting this method could be highly accurate in distinguishing the two, pending future confirmatory studies.

PET scans may also help identify true progression (Fig. 7.7). MET PET shows higher uptake in metastases compared to radiation necrosis, with a sensitivity of 79% and specificity of 75% (Terakawa et al., 2008). FET uptake is well correlated with MET uptake ($r = 0.84$) and also appears to distinguish true progression from radiation changes (Grosu et al., 2011). In addition to static PET images, dynamic PET following injection of FET has been investigated. Galldiks and colleagues (2012) report the highest diagnostic accuracy (93%) when combining mean tumor-to-brain ratio (> 1.9) and specific curve patterns from dynamic imaging, first in a pilot study of $n = 40$ lesions and subsequently confirmatory study of 76 metastasis (Fig. 7.8) (Ceccon et al., 2016). Similar accuracy (sensitivity of 86% and specificity of 79% using tumor-to-brain ratio maximum, with cutoff of 2.15) has been reported in other fairly large studies ($n = 50$), which also showed added value of time–activity curves (sensitivity and specificity increased to 93% and 84% respectively) (Romagna et al., 2016).

FDOPA PET also appears to be accurate in identifying pseudoprogression (Cicone et al., 2014) and may be superior to perfusion MRI (Fig. 7.9). In a study of 46 lesions using maximum lesion standardized uptake value to maximum background ratio (cutoff of 1.59), sensitivity was 90% and specificity was 92%. This compared favorably to rCBV analysis (cutoff of 2.1), which had a sensitivity of 87% and specificity of 68%. Similar results with FDOPA PET have been reported using only visual scoring, without quantification: in a study of 83 brain metastases, sensitivity of 81%and specificity of 84% were achieved in differentiating disease progression from delayed radiation injury (Lizarraga et al., 2014).

Another approach has been to apply radiomics to this diagnostic dilemma. Radiomics quantifies a variety of MR features such as texture, shape, and heterogeneity, generating the

ability to extract a wealth of data from scans, some of which may be invisible to the unaided eye (Zhang et al., 2016; Lohmann et al., 2017). The hope is that computer algorithms can then be trained to recognize different lesions, so that classification can be done automatically, presumably resulting in less user-dependent bias. For instance, Zhang and colleagues (2016) started out with 282 radiomics features that were narrowed to 40 features taken from two time points that differed between patient scans showing radiation necrosis versus true tumor progression. The model was further narrowed to 11 features based on 10-fold crossvalidation, resulting in an AUC of 0.79 with an accuracy of 83% for distinguishing true progression from treatment effect (Zhang et al., 2016). Thus these results, achieved from standard imaging alone, were comparable to those based on PET and perfusion data. Similarly, others have shown that radiomics textural data may improve the diagnostic accuracy of FET PET, rendering the added analytic step involving dynamic scan data unnecessary (Lohmann et al., 2017).

Interestingly, some tumor characteristics may also help identify patients who are at risk of radiation necrosis, even before treatment has been initiated. For instance, in a multivariate analysis of tumor histology, size and prior whole-brain radiotherapy, and maximum tumor diameter on pretreatment scans were associated with a threefold risk of developing radiation necrosis: tumors with a diameter > 1.5 cm had incidence of 60% radiation necrosis by 2 years, which was about four times that of tumors < 0.5 cm (Kohutek et al., 2015). Another study with a very large sample size (n = 2200 brain metastasis) also found that size, as well as a renal primary tumor, was associated with increased risk of developing radionecrosis after SRS (Sneed et al., 2015).

Another interesting phenomenon is the pattern of imaging changes that occurs when the vascular endothelial growth factor inhibitor bevacizumab is used to control edema and mass effect associated with radiation necrosis. Although first reported in gliomas (Mong et al., 2012), a similar finding of persistent restricted diffusion also can occur in patients with brain metastases who are then treated with bevacizumab after developing radiation necrosis (Delishaj et al., 2015; Fabiano and Fanous, 2016) (Fig. 7.10).

Immunotherapy

Biologic treatments such as immunotherapy or antibody-based therapies can also elicit imaging changes that may be confused with tumor recurrence or progression. Immune therapy increases the incidence of radiation necrosis after treatment of brain metastases with SRS (Colaco et al., 2016). Increased rates of hemorrhage of melanoma brain metastases treated with whole-brain radiotherapy and ipilimumab have also been reported (Gerber et al., 2015). In one case report, brain melanoma metastases appeared to progress by imaging only 11 days after treatment with the PD-1 inhibitor pembrolizumab, but surgically resected lesions showed only treatment-related change rather than viable tumor (Cohen et al., 2015) Potentially FET PET could have a role in distinguishing true from pseudoprogression in the setting of immunotherapy. In a very small study in melanoma patients with brain metastases treated with immune checkpoint inhibition, maximum tumor to normal brain ratio calculated from FET PET scans was 2.5 in the single pseudoprogressor but ranged from 2.9 to 8.6 in the four true progressors (Kebir et al., 2016). It will be necessary to further characterize the

relationship between imaging biomarkers, potential pseudoprogression, and outcomes in these patients.

PREDICTING RESPONSE PRIOR TO TREATMENT INITIATION (PROGNOSTIC MARKERS)

Standard and advanced imaging features may correlate with outcome, prior to therapy initiation. Such prognostic markers could potentially aid treatment decisions. For instance, sparse edema, somewhat counterintuitively, may be associated with more tumor invasion and a poorer prognosis. Thus in patients with a single brain metastasis treated with surgical resection, improved survival is associated with abundant brain edema, whereas tumors with little brain edema appear to have a more invasive pattern of growth (Spanberger et al., 2012). Melanoma or renal histology and prior whole-brain radiotherapy predict increased edema after SRS treatment (Hanna et al., 2015), suggesting these patients may need to be more carefully monitored for development of mass effect. High lesion mean ADC in patients with single brain metastases is associated with longer survival (30 vs. 7 months) (Berghoff et al., 2013b). Similar findings have been reported by others (Zakaria et al., 2014). High FLAIR signal in the resection cavity in postoperative patients may indicate impending local recurrence after neurosurgical resection (Bette et al., 2016a). Conversely, neither pretreatment CBV (Essig et al., 2003) nor MRS is predictive of response to radiosurgery (Chernov et al., 2007). It is hoped that the combination of these or similar prognostic markers with predictive and early response markers will help optimize treatment for patients with brain metastases.

CONCLUSIONS

MRI has exquisite sensitivity for the detection of brain tumors of all kinds and remains the modality of choice to identify brain metastases and monitor their response to treatment. A vast expansion of MR capabilities has led to a wealth of physiologic and imaging biomarkers that may add value to standard MR, based on newfound abilities to characterize cellularity, angiogenesis, perfusion, pH, hypoxia, and other features of normal and abnormal cellular growth and metabolism. These tools may enhance the diagnosis and monitoring of patients with brain metastases as they progress through treatment and may allow imaging to further improve patient outcomes. Advanced imaging, including perfusion, diffusion, and MRS of peritumoral regions, may help differentiate primary from metastatic disease, and perfusion and amino acid PET are proving to be valuable adjuvants to standard imaging in distinguishing radiation necrosis from treatment effect. Standardization and validation of these biomarkers, potentially employing automated and multiparametric modeling based on both MR and PET data, are ongoing endeavors that need to be streamlined to increase the throughput from discovery to validation, allowing robust markers targeted to specific applications to be meaningfully integrated into clinical practice.

References

Abdoli M, Chakraborty S, MacLean HJ et al. (2016). The evaluation of MRI diffusion values of active demyelinating lesions in multiple sclerosis. Mult Scler Relat Disord 10: 97–102. [PubMed: 27919508]

Abe T, Mizobuchi Y, Sako W et al. (2015). Clinical significance of discrepancy between arterial spin labeling images and contrast-enhanced images in the diagnosis of brain tumors. Magn Reson Med Sci 14: 313–319. [PubMed: 26104074]

Almeida-Freitas DB, Pinho MC, Otaduy MCG et al. (2014). Assessment of irradiated brain metastases using dynamic contrast-enhanced magnetic resonance imaging. Neuroradiology 56: 437–443. [PubMed: 24652530]

Ambrosini RD, Wang P, O'Dell WG (2010). Computer-aided detection of metastatic brain tumors using automated threedimensional template matching. J Magn Reson Imaging 31: 85–93. [PubMed: 20027576]

Anzalone N, Essig M, Lee SK et al. (2013). Optimizing contrast-enhanced magnetic resonance imaging characterization of brain metastases: relevance to stereotactic radiosurgery. Neurosurgery 72: 691–701. [PubMed: 23381488]

Baliyan V, Das CJ, Sharma R et al. (2016). Diffusion weighted imaging: technique and applications. World J Radiol 8: 785–798. [PubMed: 27721941]

Barajas RF, Jr, Cha S (2012). Imaging diagnosis of brain metastasis. Prog Neurol Surg 25: 55–73. [PubMed: 22236668]

Barajas RF, Chang JS, Sneed PK et al. (2009). Distinguishing recurrent intra-axial metastatic tumor from radiation necrosis following gamma knife radiosurgery using dynamic susceptibility-weighted contrast-enhanced perfusion MR imaging. AJNR Am J Neuroradiol 30: 367–372. [PubMed: 19022867]

Ba-Ssalamah A, Nobauer-Huhmann IM, Pinker K et al. (2003). Effect of contrast dose and field strength in the magnetic resonance detection of brain metastases. Invest Radiol 38: 415–422. [PubMed: 12821855]

Bauer AH, Erly W, Moser FG et al. (2015). Differentiation of solitary brain metastasis from glioblastoma multiforme: a predictive multiparametric approach using combined MR diffusion and perfusion. Neuroradiology 57: 697–703. [PubMed: 25845813]

Berghoff AS, Rajky O, Winkler F et al. (2013a). Invasion patterns in brain metastases of solid cancers. Neuro-Oncology 15: 1664–1672. [PubMed: 24084410]

Berghoff AS, Spanberger T, Ilhan-Mutlu A et al. (2013b). Preoperative diffusion-weighted imaging of single brain metastases correlates with patient survival times. PLoS ONE 8: e55464. [PubMed: 23393579]

Bette S, Gempt J, Wiestler B et al. (2016a). Increase in FLAIR signal of the fluid within the resection cavity as early recurrence marker: also valid for brain metastases? RöFo-Fortschritte auf dem Gebiet der Röntgenstrahlen und der bildgebenden Verfahren 189: 63–70.

Bette S, Huber T, Wiestler B et al. (2016b). Analysis of fractional anisotropy facilitates differentiation of glioblastoma and brain metastases in a clinical setting. Eur J Radiol 85: 2182–2187. [PubMed: 27842664]

Blasel S, Jurcoane A, Franz K et al. (2010). Elevated peritumoural rCBV values as a mean to differentiate metastases from high-grade gliomas. Acta Neurochir (Wien) 152: 1893–1899. [PubMed: 20799046]

Boxerman JL, Shiroishi MS, Ellingson BM et al. (2016). Dynamic susceptibility contrast MR imaging in glioma: review of current clinical practice. Magn Reson Imaging Clin N Am 24: 649–670. [PubMed: 27742108]

Brandao LA, Castillo M (2016). Adult brain tumors: clinical applications of magnetic resonance spectroscopy. Magn Reson Imaging Clin N Am 24: 781–809. [PubMed: 27742117]

Bukte Y, Paksoy Y, Genc E et al. (2005). Role of diffusion-weighted MR in differential diagnosis of intracranial cystic lesions. Clin Radiol 60: 375–383. [PubMed: 15710142]

Bulakbasi N, Guvenc I, Onguru O et al. (2004). The added value of the apparent diffusion coefficient calculation to magnetic resonance imaging in the differentiation and grading of malignant brain tumors. J Comput Assist Tomogr 28: 735–746. [PubMed: 15538145]

Bulakbasi N, Kocaoglu M, Farzaliyev A et al. (2005). Assessment of diagnostic accuracy of perfusion MR imaging in primary and metastatic solitary malignant brain tumors. AJNR Am J Neuroradiol 26: 2187–2199. [PubMed: 16219821]

Byrnes TJ, Barrick TR, Bell BA et al. (2011). Diffusion tensor imaging discriminates between glioblastoma and cerebral metastases in vivo. NMR Biomed 24: 54–60. [PubMed: 20665905]

Ceccon G, Lohmann P, Stoffels G et al. (2016). Dynamic O-(2-18F-fluoroethyl)-L-tyrosine positron emission tomography differentiates brain metastasis recurrence from radiation injury after radiotherapy. Neuro-Oncology 19: 281–288.

Chakraborty PS, Kumar R, Tripathi M et al. (2015). Detection of brain metastasis with 68Ga-labeled PSMA ligand PET/CT. Clin Nucl Med 40: 328–329. [PubMed: 25674861]

Chamberlain M, Junck L, Brandsma D et al. (2017). Leptomeningeal metastases: a RANO proposal for response criteria. Neuro-Oncology 19: 484–492. [PubMed: 28039364]

Chernov MF, Ono Y, Kubo O et al. (2006). Comparison of 1H-MRS-detected metabolic characteristics in single metastatic brain tumors of different origin. Brain Tumor Pathol 23: 35–40. [PubMed: 18095117]

Chernov M, Hayashi M, Izawa M et al. (2007). Metabolic characteristics of intracranial metastases, detected by single-voxel proton magnetic resonance spectroscopy, are seemingly not predictive for tumor response to gamma knife radiosurgery. Minim Invasive Neurosurg 50: 233–238. [PubMed: 17948183]

Chiang IC, Kuo Y-T, Lu C-Y et al. (2004). Distinction between high-grade gliomas and solitary metastases using peritumoral 3-T magnetic resonance spectroscopy, diffusion, and perfusion imagings. Neuroradiology 46: 619–627. [PubMed: 15243726]

Chuang MT, Liu YS, Tsai YS et al. (2016). Differentiating radiation-induced necrosis from recurrent brain tumor using MR perfusion and spectroscopy: a meta-analysis. PLoS One 11: e0141438. [PubMed: 26741961]

Cicone F, Minniti G, Romano A et al. (2014). Accuracy of F-DOPA PET and perfusion-MRI for differentiating radionecrotic from progressive brain metastases after radiosurgery. Eur J Nucl Med Mol Imaging 42: 103–111. [PubMed: 25182751]

Cohen JV, Alomari AK, Vortmeyer AO et al. (2015). Melanoma brain metastasis pseudoprogression after pembrolizumab treatment. Cancer Immun Research 4: 179–182.

Cohen-Inbar O, Xu Z, Dodson B et al. (2016). Time-delayed contrast-enhanced MRI improves detection of brain metastases: a prospective validation of diagnostic yield. J Neurooncol 130: 485–494. [PubMed: 27568036]

Colaco RJ, Martin P, Kluger HM et al. (2016). Does immunotherapy increase the rate of radiation necrosis after radiosurgical treatment of brain metastases? J Neurosurg 125: 17–23. [PubMed: 26544782]

Crisi G, Orsingher L, Filice S (2013). Lipid and macromolecules quantitation in differentiating glioblastoma from solitary metastasis: a short-echo time single-voxel magnetic resonance spectroscopy study at 3 T. J Comput Assist Tomogr 37: 265–271. [PubMed: 23493217]

Delishaj D, Ursino S, Pasqualetti F et al. (2015). The effectiveness of bevacizumab in radionecrosis after radiosurgery of a single brain metastasis. Rare Tumors 7: 6018. [PubMed: 26788278]

Devos A, Lukas L, Suykens JA et al. (2004). Classification of brain tumours using short echo time 1H MR spectra. J Magn Reson 170: 164–175. [PubMed: 15324770]

Dijkers EC, Oude Munnink TH, Kosterink JG et al. (2010). Biodistribution of 89Zr-trastuzumab and PET imaging of HER2-positive lesions in patients with metastatic breast cancer. Clin Pharmacol Ther 87: 586–592. [PubMed: 20357763]

Ding Y, Xing Z, Liu B et al. (2014). Differentiation of primary central nervous system lymphoma from high-grade glioma and brain metastases using susceptibility-weighted imaging. Brain and Behavior 4: 841–849. [PubMed: 25365807]

Duygulu G, Ovali GY, Çalli C et al. (2010). Intracerebral metastasis showing restricted diffusion: correlation with histopathologic findings. Eur J Radiol 74: 117–120. [PubMed: 19359117]

Egelhoff JC, Ross JS, Modic MT et al. (1992). MR imaging of metastatic GI adenocarcinoma in brain. AJNR Am J Neuroradiol 13: 1221–1224. [PubMed: 1636540]

Elster AD, Chen MY (1992). Can nonenhancing white matter lesions in cancer patients be disregarded? AJNR Am J Neuroradiol 13: 1309–1315. discussion 1316–1308. [PubMed: 1414820]

Ercan N, Gultekin S, Celik H et al. (2004). Diagnostic value of contrast-enhanced fluid-attenuated inversion recovery MR imaging of intracranial metastases. AJNR Am J Neuroradiol 25: 761–765. [PubMed: 15140715]

Essig M, Waschkies M, Wenz F et al. (2003). Assessment of brain metastases with dynamic susceptibility-weighted contrast-enhanced MR imaging: initial results. Radiology 228: 193–199. [PubMed: 12832582]

Fabiano A, Fanous A (2016). Bevacizumab for the treatment of post-stereotactic radiosurgery adverse radiation effect. Surg Neurol International 7: 542.

Feng W, Zhang P, Zheng X et al. (2014). Neuroimaging and clinical characteristics of brain metastases from esophageal carcinoma in Chinese patients. Journal of Cancer Research and Therapeutics 10: 296. [PubMed: 25693939]

Floriano VH, Torres US, Spotti AR et al. (2013). The role of dynamic susceptibility contrast-enhanced perfusion MR imaging in differentiating between infectious and neoplastic focal brain lesions: results from a cohort of 100 consecutive patients. PLoS One 8: e81509. [PubMed: 24324699]

Franceschi AM, Moschos SJ, Anders CK et al. (2016). Use of susceptibility-weighted imaging (SWI) in the detection of brain hemorrhagic metastases from breast cancer and melanoma. J Comput Assist Tomogr 40: 803–805. [PubMed: 27636126]

Fraum TJ, Ludwig DR, Bashir MR et al. (2017). Gadolinium-based contrast agents: a comprehensive risk assessment. J Magn Reson Imaging 46: 338–353. [PubMed: 28083913]

Galldiks N, Stoffels G, Filss CP et al. (2012). Role of O-(2-18F-fluoroethyl)-L-tyrosine PET for differentiation of local recurrent brain metastasis from radiation necrosis. J Nucl Med 53: 1367–1374. [PubMed: 22872742]

Galldiks N, Langen KJ, Pope WB (2015). From the clinician's point of view – what is the status quo of positron emission tomography in patients with brain tumors? Neuro Oncol 17: 1434–1444. [PubMed: 26130743]

Gaviani P, Mullins ME, Braga TA et al. (2006). Improved detection of metastatic melanoma by T2*-weighted imaging. AJNR Am J Neuroradiol 27: 605–608. [PubMed: 16552002]

Gaykema SBM, Brouwers AH, Lub-de Hooge MN et al. (2013). 89Zr-bevacizumab PET imaging in primary breast cancer. J Nucl Med 54: 1014–1018. [PubMed: 23651946]

Geijer B, Holtas S (2002). Diffusion-weighted imaging of brain metastases: their potential to be misinterpreted as focal ischaemic lesions. Neuroradiology 44: 568–573. [PubMed: 12136357]

Gempt J, Bette S, Buchmann N et al. (2015). Volumetric analysis of F-18-FET-PET imaging for brain metastases. World Neurosurgery 84: 1790–1797. [PubMed: 26255241]

Georgiadis P, Cavouras D, Kalatzis I et al. (2008). Improving brain tumor characterization on MRI by probabilistic neural networks and non-linear transformation of textural features. Comput Methods Programs Biomed 89: 24–32. [PubMed: 18053610]

Gerber NK, Young RJ, Barker CA et al. (2015). Ipilimumab and whole brain radiation therapy for melanoma brain metastases. J Neurooncol 121: 159–165. [PubMed: 25273687]

Gil B, Hwang EJ, Lee S et al. (2016). Detection of leptomeningeal metastasis by contrast-enhanced 3D T1-SPACE: comparison with 2D FLAIR and contrast-enhanced 2D T1-weighted images. PLoS One 11: e0163081. [PubMed: 27695096]

Grade M, Hernandez Tamames JA, Pizzini FB et al. (2015). A neuroradiologist's guide to arterial spin labeling MRI in clinical practice. Neuroradiology 57: 1181–1202. [PubMed: 26351201]

Graif M, Bydder GM, Steiner RE et al. (1985). Contrast-enhanced MR imaging of malignant brain tumors. AJNR Am J Neuroradiol 6: 855–862. [PubMed: 3934926]

Griffith B, Jain R (2016). Perfusion imaging in neurooncology: basic techniques and clinical applications. Magn Reson Imaging Clin N Am 24: 765–779. [PubMed: 27742116]

Grosu AL, Astner ST, Riedel E et al. (2011). An interindividual comparison of O-(2-[18F]fluoroethyl)-L-tyrosine (FET)- and L-[methyl-11C]methionine (MET)-PET in patients with brain gliomas and metastases. Int J Radiat Oncol Biol Phys 81: 1049–1058. [PubMed: 21570201]

Hakyemez B, Erdogan C, Yildirim N et al. (2005). Glioblastoma multiforme with atypical diffusion-weighted MR findings. Br J Radiol 78: 989–992. [PubMed: 16249598]

Han C, Huang S, Guo J et al. (2014). Use of a high b-value for diffusion weighted imaging of peritumoral regions to differentiate high-grade gliomas and solitary metastases. J Magn Reson Imaging 42: 80–86. [PubMed: 25223489]

Hanna A, Boggs DH, Kwok Y et al. (2015). What predicts early volumetric edema increase following stereotactic radiosurgery for brain metastases? J Neurooncol 127: 303–311. [PubMed: 26721241]

Harris RJ, Cloughesy TF, Liau LM et al. (2015). pH-weighted molecular imaging of gliomas using amine chemical exchange saturation transfer MRI. Neuro Oncol 17: 1514–1524. [PubMed: 26113557]

Harris RJ, Cloughesy TF, Liau LM et al. (2016). Simulation, phantom validation, and clinical evaluation of fast pH-weighted molecular imaging using amine chemical exchange saturation transfer echo planar imaging (CEST-EPI) in glioma at 3 T. NMR Biomed 29: 1563–1576. [PubMed: 27717216]

Hartmann M, Jansen O, Heiland S et al. (2001). Restricted diffusion within ring enhancement is not pathognomonic for brain abscess. AJNR Am J Neuroradiol 22: 1738–1742. [PubMed: 11673170]

Hatzoglou V, Yang TJ, Omuro A et al. (2015). A prospective trial of dynamic contrast-enhanced MRI perfusion and fluorine-18 FDG PET-CT in differentiating brain tumor progression from radiation injury after cranial irradiation. Neuro-Oncology 18: 873–880. [PubMed: 26688076]

Hatzoglou V, Karimi S, Diamond EL et al. (2016). Nonenhancing leptomeningeal metastases. The Neurohospitalist 6: 24–28. [PubMed: 26753054]

Hayashida Y, Hirai T, Morishita S et al. (2006). Diffusion-weighted imaging of metastatic brain tumors: comparison with histologic type and tumor cellularity. AJNR Am J Neuroradiol 27: 1419–1425. [PubMed: 16908550]

Hoefnagels FWA, Lagerwaard FJ, Sanchez E et al. (2009). Radiological progression of cerebral metastases after radiosurgery: assessment of perfusion MRI for differentiating between necrosis and recurrence. J Neurol 256: 878–887. [PubMed: 19274425]

Huang BY, Kwock L, Castillo M et al. (2010). Association of choline levels and tumor perfusion in brain metastases assessed with proton MR spectroscopy and dynamic susceptibility contrast-enhanced perfusion weighted MRI. Technol Cancer Res Treat 9: 327–337. [PubMed: 20626199]

Huang J, Wang AM, Shetty A et al. (2011). Differentiation between intra-axial metastatic tumor progression and radiation injury following fractionated radiation therapy or stereotactic radiosurgery using MR spectroscopy, perfusion MR imaging or volume progression modeling. Magn Reson Imaging 29: 993–1001. [PubMed: 21571478]

Hutterer M, Nowosielski M, Putzer D et al. (2013). [18F]-fluoro-ethyl-L-tyrosine PET: a valuable diagnostic tool in neuro-oncology, but not all that glitters is glioma. Neuro-Oncology 15: 341–351. [PubMed: 23335162]

Hutterer M, Ebner Y, Riemenschneider MJ et al. (2017). Epileptic activity increases cerebral amino acid transport assessed by 18F-fluoroethyl-l-tyrosine amino acid PET: a potential brain tumor mimic. J Nucl Med 58: 129–137. [PubMed: 27469356]

Isiklar I, Leeds NE, Fuller GN et al. (1995). Intracranial metastatic melanoma: correlation between MR imaging characteristics and melanin content. AJR Am J Roentgenol 165: 1503–1512. [PubMed: 7484597]

Jakubovic R, Sahgal A, Soliman H et al. (2014). Magnetic resonance imaging-based tumour perfusion parameters are biomarkers predicting response after radiation to brain metastases. Clin Oncol 26: 704–712.

Jakubovic R, Zhou S, Heyn C et al. (2016). The predictive capacity of apparent diffusion coefficient (ADC) in response assessment of brain metastases following radiation. Clin Exp Metastasis 33: 277–284. [PubMed: 26786978]

Jones T, Rabiner EA, Company PETRA (2012). The development, past achievements, and future directions of brain PET. J Cereb Blood Flow Metab 32: 1426–1454. [PubMed: 22434067]

Juhasz C, Dwivedi S, Kamson DO et al. (2014). Comparison of amino acid positron emission tomographic radiotracers for molecular imaging of primary and metastatic brain tumors. Mol Imaging 13: 13.

Kamalian S, Lev MH, Gupta R (2016). Computed tomography imaging and angiography – principles. Handb Clin Neurol 135: 3–20. [PubMed: 27432657]

Kamson DO, Mittal S, Buth A et al. (2013). Differentiation of glioblastomas from metastatic brain tumors by tryptophan uptake and kinetic analysis: a positron emission tomographic study with magnetic resonance imaging comparison. Mol Imaging 12: 327–337. [PubMed: 23759373]

Kebir S, Rauschenbach L, Galldiks N et al. (2016). Dynamic O-(2-[18F]fluoroethyl)-L-tyrosine PET imaging for the detection of checkpoint inhibitor-related pseudoprogression in melanoma brain metastases. Neuro Oncol 18: 1462–1464. [PubMed: 27591333]

Kohutek ZA, Yamada Y, Chan TA et al. (2015). Long-term risk of radionecrosis and imaging changes after stereotactic radiosurgery for brain metastases. J Neurooncol 125: 149–156. [PubMed: 26307446]

Krautmacher C, Willinek WA, Tschampa HJ et al. (2005). Brain tumors: full- and half-dose contrast-enhanced MR imaging at 3.0 T compared with 1.5 T – initial experience. Radiology 237: 1014–1019. [PubMed: 16237142]

Krüger S, Mottaghy FM, Buck AK et al. (2010). Brain metastasis in lung cancer. Nuklearmedizin 50: 101–106. [PubMed: 21165538]

Kunikowska J, Pawlak D, Kolasa A et al. (2014). A frequency and semiquantitative analysis of pathological 68Ga DOTATATE PET/CT uptake by primary site-dependent neuroendocrine tumor metastasis. Clin Nucl Med 39: 855–861. [PubMed: 25072928]

Kushnirsky M, Nguyen V, Katz JS et al. (2016). Time-delayed contrast-enhanced MRI improves detection of brain metastases and apparent treatment volumes. J Neurosurg 124: 489–495. [PubMed: 26361281]

Kwak H-S, Hwang S, Chung G-H et al. (2015). Detection of small brain metastases at 3 T: comparing the diagnostic performances of contrast-enhanced T1-weighted SPACE, MPRAGE, and 2D FLASH imaging. Clin Imaging 39: 571–575. [PubMed: 25770904]

Lee C-C, Wintermark M, Xu Z et al. (2014). Application of diffusion-weighted magnetic resonance imaging to predict the intracranial metastatic tumor response to gamma knife radiosurgery. J Neurooncol 118: 351–361. [PubMed: 24760414]

Liang R, Wang X, Li M et al. (2014). Meta-analysis of peritumoural rCBV values derived from dynamic susceptibility contrast imaging in differentiating high-grade gliomas from intracranial metastases. Int J Clin Exp Med 7: 2724–2729. [PubMed: 25356131]

Lin JP, Kricheff II, Laguna J et al. (1976). Brain tumors studied by computerized tomography. Adv Neurol 15: 175–199. [PubMed: 937153]

Lin NU, Lee EQ, Aoyama H et al. (2015). Response assessment criteria for brain metastases: proposal from the RANO group. Lancet Oncol 16: e270–e278. [PubMed: 26065612]

Lin L, Xue Y, Duan Q et al. (2016). The role of cerebral blood flow gradient in peritumoral edema for differentiation of glioblastomas from solitary metastatic lesions. Oncotarget 7: 69051–69059. [PubMed: 27655705]

Lin X, Lee M, Buck O et al. (2017). Diagnostic accuracy of T1-weighted dynamic contrast-enhanced-MRI and DWI-ADC for differentiation of glioblastoma and primary CNS lymphoma. AJNR Am J Neuroradiol 38: 485–491. [PubMed: 27932505]

Lizarraga KJ, Allen-Auerbach M, Czernin J et al. (2014). (18) F-FDOPA PET for differentiating recurrent or progressive brain metastatic tumors from late or delayed radiation injury after radiation treatment. J Nucl Med 55: 30–36. [PubMed: 24167081]

Lohmann P, Stoffels G, Ceccon G et al. (2017). Radiation injury vs. recurrent brain metastasis: combining textural feature radiomics analysis and standard parameters may increase 18F-FET PET accuracy without dynamic scans. Eur Radiol 27: 2916–2927. [PubMed: 27853813]

Longo DL, Bartoli A, Consolino L et al. (2016). In vivo imaging of tumor metabolism and acidosis by combining PET and MRI-CEST pH imaging. Cancer Res 76: 6463–6470. [PubMed: 27651313]

Lu S, Ahn D, Johnson G et al. (2003). Peritumoral diffusion tensor imaging of high-grade gliomas and metastatic brain tumors. AJNR Am J Neuroradiol 24: 937–941. [PubMed: 12748097]

Malikova H, Koubska E, Weichet J et al. (2016). Can morphological MRI differentiate between primary central nervous system lymphoma and glioblastoma? Cancer Imaging 16: 40. [PubMed: 27894359]

Maroldi R, Ambrosi C, Farina D (2005). Metastatic disease of the brain: extra-axial metastases (skull, dura, leptomeningeal) and tumour spread. Eur Radiol 15: 617–626. [PubMed: 15627175]

Masdeu JC, Quinto C, Olivera C et al. (2000). Open-ring imaging sign: highly specific for atypical brain demyelination. Neurology 54: 1427–1433. [PubMed: 10751251]

Mehrabian H, Desmond KL, Soliman H et al. (2017). Differentiation between radiation necrosis and tumor progression using chemical exchange saturation transfer. Clin Cancer Res 23: 3667–3675. [PubMed: 28096269]

Meyer H-J, Fiedler E, Kornhuber M et al. (2015). Comparison of diffusion-weighted imaging findings in brain metastases of different origin. Clinical Imaging 39: 965–969. [PubMed: 26253774]

Miquelini LA, Pérez Akly MS, Funes JA et al. (2016). Usefulness of the apparent diffusion coefficient for the evaluation of the white matter to differentiate between glioblastoma and brain metastases. Radiología (English Edition) 58: 207–213.

Mitsuya K, Nakasu Y, Horiguchi S et al. (2010). Perfusion weighted magnetic resonance imaging to distinguish the recurrence of metastatic brain tumors from radiation necrosis after stereotactic radiosurgery. J Neurooncol 99: 81–88. [PubMed: 20058049]

Momose T, Nariai T, Kawabe T et al. (2014). Clinical benefit of 11C methionine PET imaging as a planning modality for radiosurgery of previously irradiated recurrent brain metastases. Clin Nucl Med 39: 939–943. [PubMed: 25140562]

Mong S, Ellingson BM, Nghiemphu PL et al. (2012). Persistent diffusion-restricted lesions in bevacizumab-treated malignant gliomas are associated with improved survival compared with matched controls. AJNR Am J Neuroradiol 33: 1763–1770. [PubMed: 22538078]

Noebauer-Huhmann IM, Szomolanyi P, Kronnerwetter C et al. (2015). Brain tumours at 7T MRI compared to 3T – contrast effect after half and full standard contrast agent dose: initial results. Eur Radiol 25: 106–112. [PubMed: 25194707]

Nussbaum ES, Djalilian HR, Cho KH et al. (1996). Brain metastases. Histology, multiplicity, surgery, and survival. Cancer 78: 1781–1788. [PubMed: 8859192]

Ohno Y, Koyama H, Nogami M et al. (2007). Whole-body MR imaging vs. FDG-PET: comparison of accuracy of M-stage diagnosis for lung cancer patients. J Magn Reson Imaging 26: 498–509. [PubMed: 17729341]

Okubo T, Hayashi N, Shirouzu I et al. (1998). Detection of brain metastasis: comparison of turbo-FLAIR imaging, T2-weighted imaging and double-dose gadolinium-enhanced MR imaging. Radiat Med 16: 273–281. [PubMed: 9814422]

O'Sullivan CC, Lindenberg M, Bryla C et al. (2016). ANG1005 for breast cancer brain metastases: correlation between 18F-FLT-PET after first cycle and MRI in response assessment. Breast Cancer Res Treat 160: 51–59. [PubMed: 27620882]

Packer RJ, Schiff D (2012). Neuro-oncology, Wiley-Blackwell, Chichester, West Sussex.

Patchell RA, Tibbs PA, Walsh JW et al. (1990). A randomized trial of surgery in the treatment of single metastases to the brain. N Engl J Med 322: 494–500. [PubMed: 2405271]

Patel TR, McHugh BJ, Bi WL et al. (2011). A comprehensive review of MR imaging changes following radiosurgery to 500 brain metastases. AJNR Am J Neuroradiol 32: 1885–1892. [PubMed: 21920854]

Patel SH, Robbins JR, Gore EM et al. (2012). ACR Appropriateness Criteria follow-up and retreatment of brain metastases. Am J Clin Oncol 35: 302–306. [PubMed: 22609733]

Pavlisa G, Rados M, Pavlisa G et al. (2009). The differences of water diffusion between brain tissue infiltrated by tumor and peritumoral vasogenic edema. Clinical Imaging 33: 96–101. [PubMed: 19237051]

Polyzoidis KS, Miliaras G, Pavlidis N (2005). Brain metastasis of unknown primary: a diagnostic and therapeutic dilemma. Cancer Treat Rev 31: 247–255. [PubMed: 15913895]

Quattrocchi CC, Errante Y, Gaudino C et al. (2012). Spatial brain distribution of intra-axial metastatic lesions in breast and lung cancer patients. J Neurooncol 110: 79–87. [PubMed: 22802020]

Radbruch A, Graf M, Kramp L et al. (2012). Differentiation of brain metastases by percentagewise quantification of intratumoral-susceptibility-signals at 3Tesla. Eur J Radiol 81: 4064–4068. [PubMed: 22795527]

Rapalino O, Ratai EM (2016). Multiparametric imaging analysis: magnetic resonance spectroscopy. Magn Reson Imaging Clin N Am 24: 671–686. [PubMed: 27742109]

Rapp M, Heinzel A, Galldiks N et al. (2013). Diagnostic performance of 18F-FET PET in newly diagnosed cerebral lesions suggestive of glioma. J Nucl Med 54: 229–235. [PubMed: 23232275]

Reddy JS, Mishra AM, Behari S et al. (2006). The role of diffusion-weighted imaging in the differential diagnosis of intracranial cystic mass lesions: a report of 147 lesions. Surg Neurol 66: 246–250. discussion 250–251. [PubMed: 16935625]

Reichert M, Morelli JN, Runge VM et al. (2013). Contrast-enhanced 3-dimensional SPACE versus MP-RAGE for the detection of brain metastases: considerations with a 32-channel head coil. Invest Radiol 48: 55–60. [PubMed: 23192164]

Rohren EM, Provenzale JM, Barboriak DP et al. (2003). Screening for cerebral metastases with FDG PET in patients undergoing whole-body staging of non-central nervous system malignancy. Radiology 226: 181–187. [PubMed: 12511688]

Romagna A, Unterrainer M, Schmid-Tannwald C et al. (2016). Suspected recurrence of brain metastases after focused high dose radiotherapy: can [18F]FET- PET overcome diagnostic uncertainties? Radiat Oncol 11: 139. [PubMed: 27769279]

Ruiz-Espana S, Jimenez-Moya A, Arana E et al. (2015). Functional diffusion map: a biomarker of brain metastases response to treatment based on magnetic resonance image analysis. In: 37th Annual International Conference of the IEEE Engineering in Medicine and Biology Society (EMBC), Electrical and Electronics Engineers (IEEE), Institute of.

Schwartz KM, Erickson BJ, Lucchinetti C (2006). Pattern of T2 hypointensity associated with ring-enhancing brain lesions can help to differentiate pathology. Neuroradiology 48: 143–149. [PubMed: 16447037]

Seidl Z, Vymazal J, Mechl M et al. (2012). Does higher gadolinium concentration play a role in the morphologic assessment of brain tumors? Results of a multicenter intraindividual crossover comparison of gadobutrol versus gadobenate dimeglumine (the MERIT Study). AJNR Am J Neuroradiol 33: 1050–1058. [PubMed: 22383237]

Server A, Josefsen R, Kulle B et al. (2010). Proton magnetic resonance spectroscopy in the distinction of high-grade cerebral gliomas from single metastatic brain tumors. Acta Radiologica 51: 316–325. [PubMed: 20092374]

Server A, Orheim TE, Graff BA et al. (2011). Diagnostic examination performance by using microvascular leakage, cerebral blood volume, and blood flow derived from 3-T dynamic susceptibility-weighted contrast-enhanced perfusion MR imaging in the differentiation of glioblastoma multiforme and brain metastasis. Neuroradiology 53: 319–330. [PubMed: 20625709]

Seute T, Leffers P, ten Velde GP et al. (2008). Detection of brain metastases from small cell lung cancer: consequences of changing imaging techniques (CT versus MRI). Cancer 112: 1827–1834. [PubMed: 18311784]

Shankar LK, Hoffman JM, Bacharach S et al. (2006). Consensus recommendations for the use of 18F-FDG PET as an indicator of therapeutic response in patients in National Cancer Institute Trials. J Nucl Med 47: 1059–1066. [PubMed: 16741317]

Singh SK, Agris JM, Leeds NE et al. (2000). Intracranial leptomeningeal metastases: comparison of depiction at FLAIR and contrast-enhanced MR imaging. Radiology 217: 50–53. [PubMed: 11012422]

Siri A, Carra-Dalliere C, Ayrignac X et al. (2015). Isolated tumefactive demyelinating lesions: diagnosis and longterm evolution of 16 patients in a multicentric study. J Neurol 262: 1637–1645. [PubMed: 25929666]

Smirniotopoulos JG, Murphy FM, Rushing EJ et al. (2007). Patterns of contrast enhancement in the brain and meninges. Radiographics 27: 525–551. [PubMed: 17374867]

Sneed PK, Mendez J, Vemer-van den Hoek JGM et al. (2015). Adverse radiation effect after stereotactic radiosurgery for brain metastases: incidence, time course, and risk factors. J Neurosurg 123: 373–386. [PubMed: 25978710]

Spanberger T, Berghoff AS, Dinhof C et al. (2012). Extent of peritumoral brain edema correlates with prognosis, tumoral growth pattern, HIF1a expression and angiogenic activity in patients with single brain metastases. Clin Exp Metastasis 30: 357–368. [PubMed: 23076770]

Sparacia G, Agnello F, Banco A et al. (2016a). Value of serial magnetic resonance imaging in the assessment of brain metastases volume control during stereotactic radiosurgery. World Journal of Radiology 8: 916. [PubMed: 28070243]

Sparacia G, Gadde JA, Iaia A et al. (2016b). Usefulness of quantitative peritumoural perfusion and proton spectroscopic magnetic resonance imaging evaluation in differentiating brain gliomas from solitary brain metastases. The Neuroradiology Journal 29: 160–167. [PubMed: 26988081]

Suh CH, Jung SC, Kim KW et al. (2016). The detectability of brain metastases using contrast-enhanced spin-echo or gradient-echo images: a systematic review and metaanalysis. J Neurooncol 129: 363–371. [PubMed: 27324495]

Sunwoo L, Yun TJ, You SH et al. (2016). Differentiation of glioblastoma from brain metastasis: qualitative and quantitative analysis using arterial spin labeling MR imaging. PLoS One 11: e0166662. [PubMed: 27861605]

Svolos P, Tsolaki E, Kapsalaki E et al. (2013). Investigating brain tumor differentiation with diffusion and perfusion metrics at 3T MRI using pattern recognition techniques. Magn Reson Imaging 31: 1567–1577. [PubMed: 23906533]

Szwarc P, Kawa J, Rudzki M et al. (2015). Automatic brain tumour detection and neovasculature assessment with multiseries MRI analysis. Comput Med Imaging Graph 46: 178–190. [PubMed: 26183648]

Terakawa Y, Tsuyuguchi N, Iwai Y et al. (2008). Diagnostic accuracy of 11C-methionine PET for differentiation of recurrent brain tumors from radiation necrosis after radiotherapy. J Nucl Med 49: 694–699. [PubMed: 18413375]

Togao O, Hiwatashi A, Yamashita K et al. (2014). Additional MR contrast dosage for radiologists' diagnostic performance in detecting brain metastases: a systematic observer study at 3 T. Jpn J Radiol 32: 537–544. [PubMed: 24957183]

Toh CH, Wei KC, Ng SH et al. (2011). Differentiation of brain abscesses from necrotic glioblastomas and cystic metastatic brain tumors with diffusion tensor imaging. AJNR Am J Neuroradiol 32: 1646–1651. [PubMed: 21835939]

Toh CH, Wei K-C, Chang C-N et al. (2014). Differentiation of brain abscesses from glioblastomas and metastatic brain tumors: comparisons of diagnostic performance of dynamic susceptibility contrast-enhanced perfusion MR imaging before and after mathematic contrast leakage correction. PLoS ONE 9: e109172. [PubMed: 25330386]

Tsolaki E, Svolos P, Kousi E et al. (2013). Automated differentiation of glioblastomas from intracranial metastases using 3T MR spectroscopic and perfusion data. Int J Comput Assist Radiol Surg 8: 751–761. [PubMed: 23334798]

Tsougos I, Svolos P, Kousi E et al. (2012). Differentiation of glioblastoma multiforme from metastatic brain tumor using proton magnetic resonance spectroscopy, diffusion and perfusion metrics at 3 T. Cancer Imaging 12: 423–436. [PubMed: 23108208]

Unterrainer M, Galldiks N, Suchorska B et al. (2017). 18F-FET PET uptake characteristics in patients with newly diagnosed and untreated brain metastasis. J Nucl Med 58: 584–589. [PubMed: 27754904]

Usinskiene J, Ulyte A, Bjornerud A et al. (2016). Optimal differentiation of high- and low-grade glioma and metastasis: a meta-analysis of perfusion, diffusion, and spectroscopy metrics. Neuroradiology 58: 339–350. [PubMed: 26767528]

Vellido A, Romero E, Julia-Sape M et al. (2012). Robust discrimination of glioblastomas from metastatic brain tumors on the basis of single-voxel (1)H MRS. NMR Biomed 25: 819–828. [PubMed: 22081447]

Wagner S, Gufler H, Eichner G et al. (2016). Characterisation of lesions after stereotactic radiosurgery for brain metastases: impact of delayed contrast magnetic resonance imaging. Clinical Oncology 29: 143–150. [PubMed: 27777145]

Weber MA, Zoubaa S, Schlieter M et al. (2006). Diagnostic performance of spectroscopic and perfusion MRI for distinction of brain tumors. Neurology 66: 1899–1906. [PubMed: 16801657]

Xu XX, Li B, Yang HF et al. (2014). Can diffusion-weighted imaging be used to differentiate brain abscess from other ring-enhancing brain lesions? A meta-analysis. Clin Radiol 69: 909–915. [PubMed: 24933524]

Yamasaki F, Kurisu K, Satoh K et al. (2005). Apparent diffusion coefficient of human brain tumors at MR imaging. Radiology 235: 985–991. [PubMed: 15833979]

Yang S, Nam Y, Kim MO et al. (2013). Computer-aided detection of metastatic brain tumors using magnetic resonance black-blood imaging. Invest Radiol 48: 113–119. [PubMed: 23211553]

Yang G, Jones TL, Howe FA et al. (2015). Morphometric model for discrimination between glioblastoma multiforme and solitary metastasis using three-dimensional shape analysis. Magn Reson Med 75: 2505–2516. [PubMed: 26173745]

Yeh R-H, Yu J-C, Chu C-H et al. (2014). Distinct MR imaging features of triple-negative breast cancer with brain metastasis. J Neuroimaging 25: 474–481. [PubMed: 25060327]

Yuh WT, Tali ET, Nguyen HD et al. (1995). The effect of contrast dose, imaging time, and lesion size in the MR detection of intracerebral metastasis. AJNR Am J Neuroradiol 16: 373–380. [PubMed: 7726087]

Zakaria R, Jenkinson MD (2014). Using ADC maps with structural scans to improve intraoperative biopsy specimens in brain metastases. The Neuroradiology Journal 27: 0.

Zakaria R, Das K, Radon M et al. (2014). Diffusion-weighted MRI characteristics of the cerebral metastasis to brain boundary predicts patient outcomes. BMC Medical Imaging 14.

Zakaria R, Pomschar A, Jenkinson MD et al. (2017). Use of diffusion-weighted MRI to modify radiosurgery planning in brain metastases may reduce local recurrence. J Neurooncol 131: 549–554. [PubMed: 27844309]

Zhang W, Ma XX, Ji YM et al. (2009). Haemorrhage detection in brain metastases of lung cancer patients using magnetic resonance imaging. J Int Med Res 37: 1139–1144. [PubMed: 19761696]

Zhang Z, Ho A, Wang X et al. (2016). TU-D-207B-01: a prediction model for distinguishing radiation necrosis from tumor progression after gamma knife radiosurgery based on radiomics features from MR images. Medical Physics 43: 3750.

Zhou C, Yang Z, Yao Z et al. (2016). Segmentation of peritumoral oedema offers a valuable radiological feature of cerebral metastasis. Br J Radiol 89: 20151054. [PubMed: 27119727]

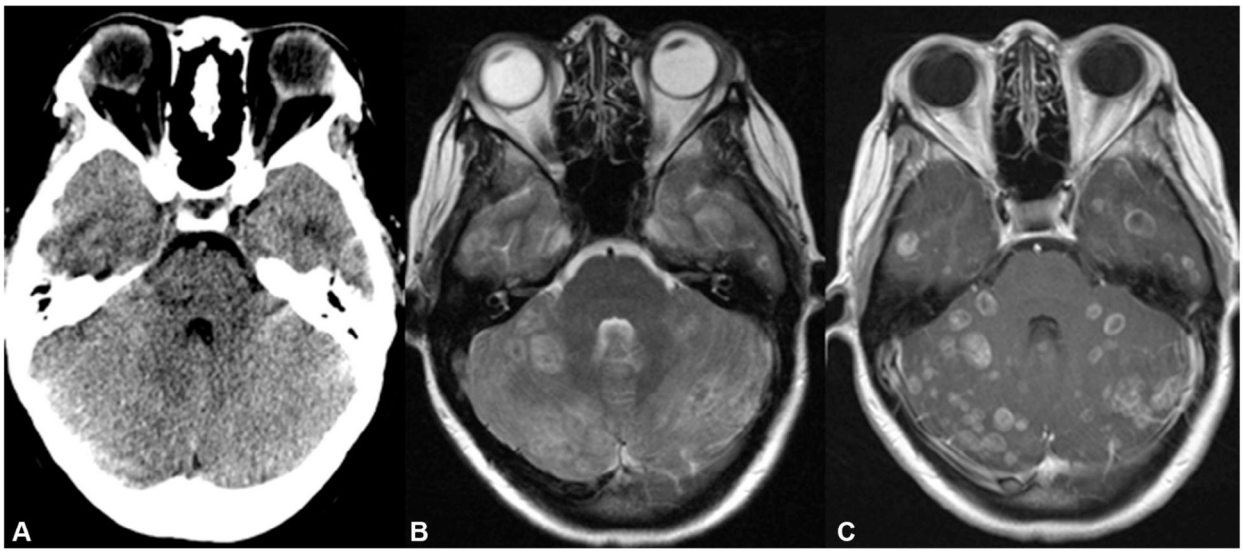

Fig. 7.1.

Noncontrast computed tomography (CT) has low sensitivity for brain metastases. A noncontrast CT image (**A**) through the posterior fossa is essentially unremarkable. T2-weighted image (**B**) of the same patient shows extensive abnormality of the cerebellum, with a very large number of metastases most clearly defined by postcontrast T1-weighted images (**C**).

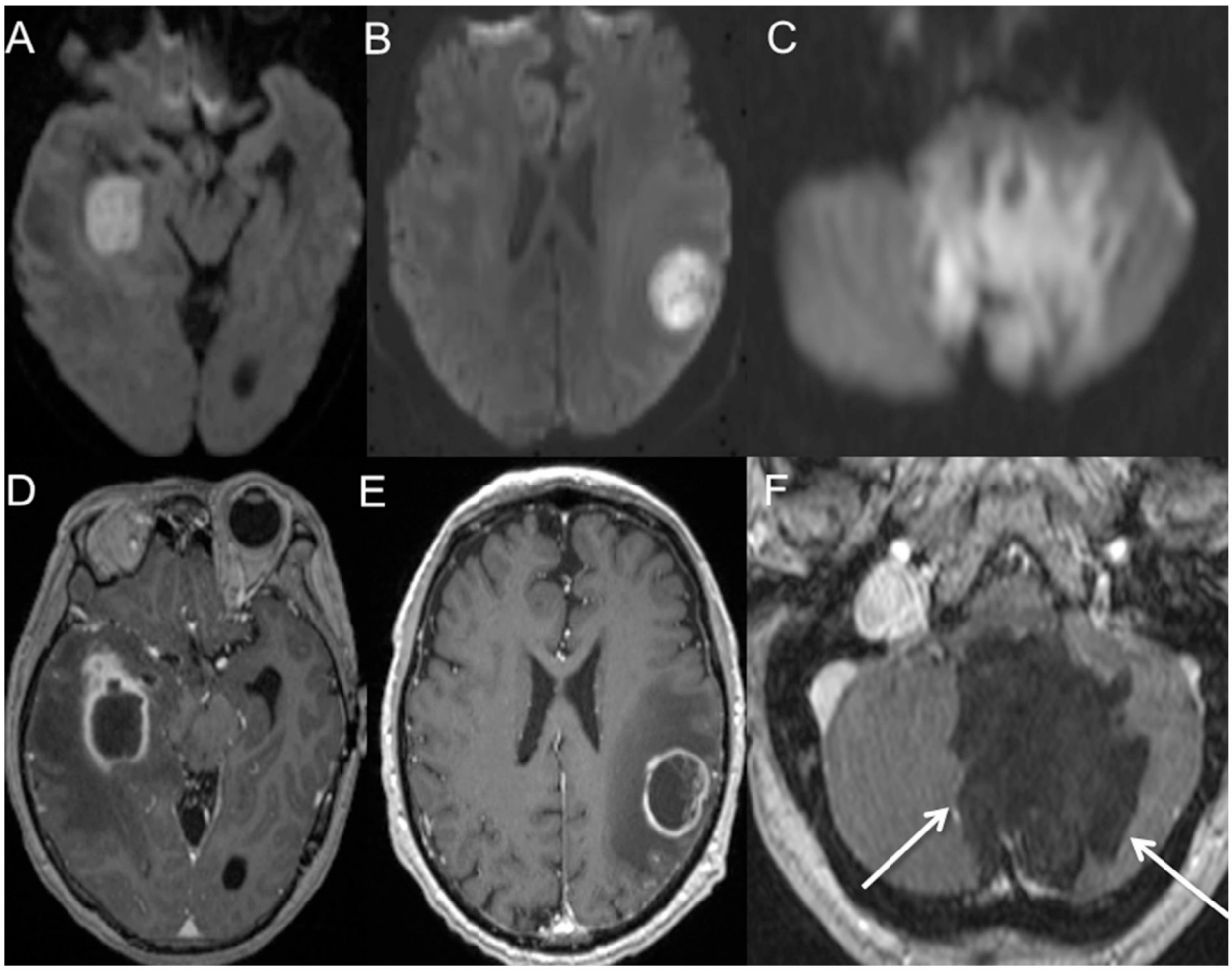

Fig. 7.2.

Abnormally restricted diffusion is a typical finding for cerebral abscess, but may occasionally occur in brain metastases. Each column represents a different patient. (**A–C**) Diffusion-weighted images; (**D–F**) postcontrast T1-weighted images. Abscess (**A**, **D**), mucinous colon metastasis (**B**, **E**), epidermoid (**C**, **F**). Note lack of enhancement at the margins of the epidermoid, unlike the other two lesions (**F**, arrows).

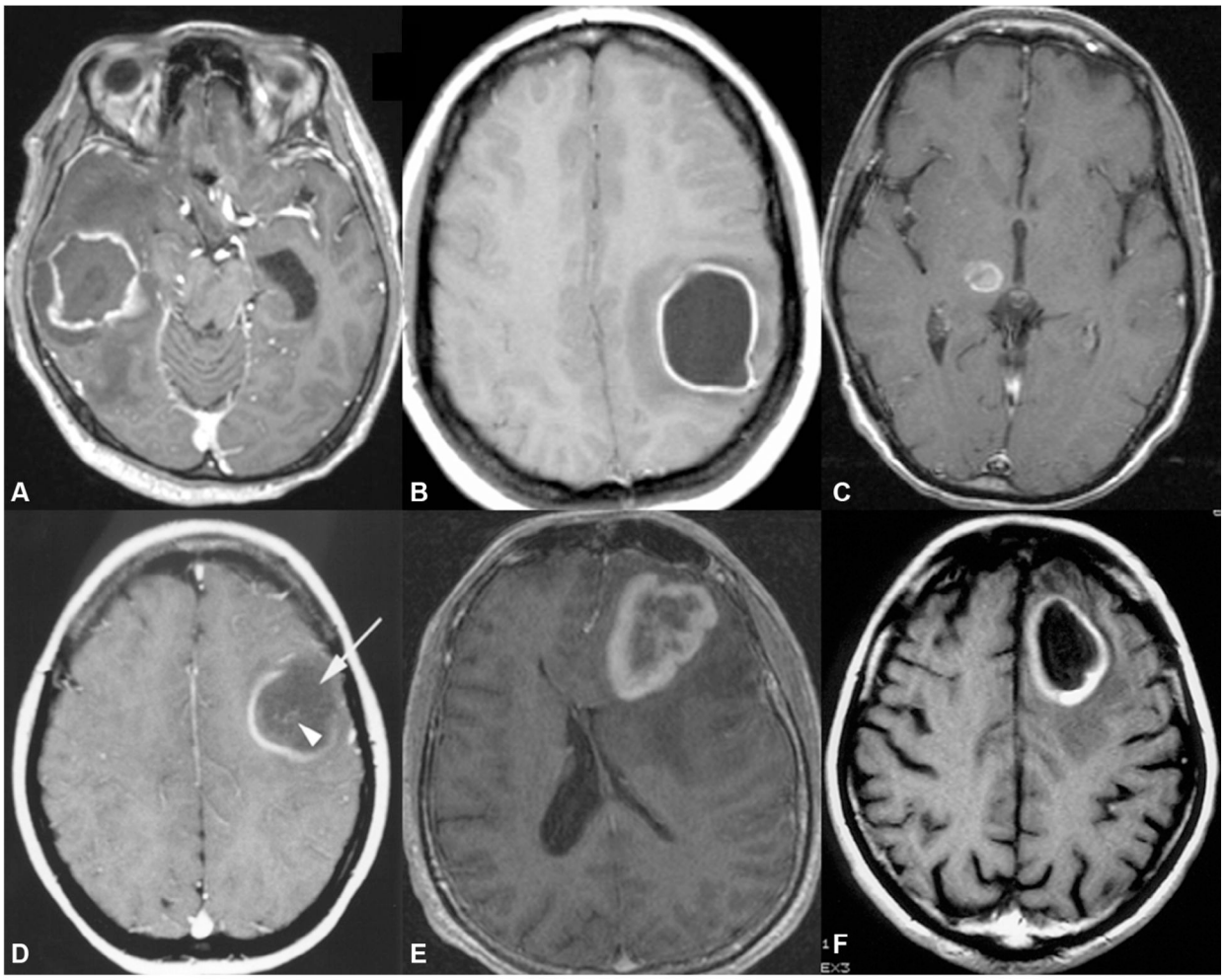

Fig. 7.3.

A wide variety of pathologies can generate a single ring-enhancing parenchymal brain lesion that resembles metastatic disease. Postcontrast T1-weighted images of the brain demonstrating (**A**) toxoplasmosis, (**B**) neurocysticercosis, (**C**) glioblastoma, (**D**) tumefactive multiple sclerosis, (**E**) lymphoma in an immunocompromised patient, and (**F**) lung carcinoma metastasis. Note incomplete ring enhancement (arrow) with some internal enhancement (arrowhead) in the patient with multiple sclerosis (**D**). This finding is suggestive of demyelinating disease.

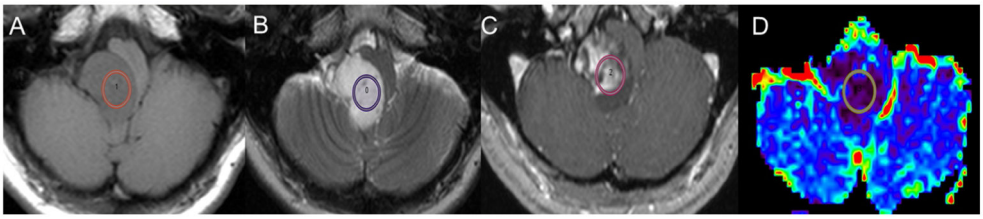

Fig. 7.4.

Perfusion imaging can help distinguish metastases from some, but not all, potential mimics. T1-weighted (**A**), T2-weighted (**B**), postcontrast T1-weighted (**C**), and cerebral blood volume map from dynamic susceptibility contrast perfusion images (**D**) of the posterior fossa with region of interest (circles) are displayed. A heterogeneously enhancing lesion in the region of the right lateral aperture of the fourth ventricle (circles) is nonspecific in appearance. However, very low relative cerebral blood volume (**D**) of 0.27 of the mass indicated a lower likelihood of metastatic disease. Neurosurgical resection followed by histopathologic analysis resulted in the diagnosis of cavernous malformation.

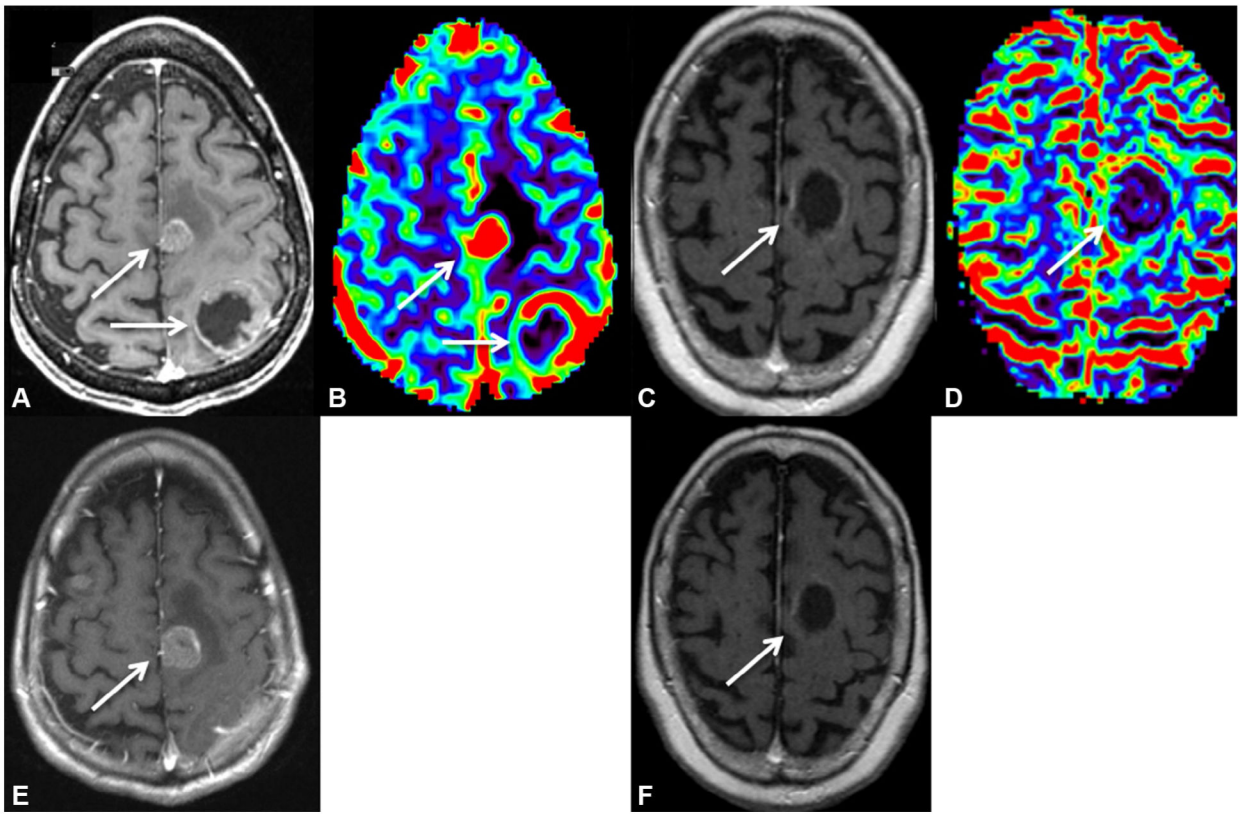

Fig. 7.5.

Potential of advanced imaging to generate early response markers after treatment. Two patients with breast brain metastases received stereotactic radiosurgery and subsequently magnetic resonance imaging with perfusion imaging 1 month later. In the first patient (**A**, **B**), a nonresponder, two enhancing lesions on the postcontrast T1-weighted image (**A**, arrows) show elevated relative cerebral blood volume (rCBV) above 3.0 (**B**). Conversely, the second patient has a ring-enhancing lesion of similar size (**C**, arrow), which shows low rCBV (< 1). Three-month follow-up images (**E**, **F**) show interval growth of one of the metastases with high rCBV (**E**, arrow). The second metastasis for this patient was resected due to increasing mass effect. Conversely, the metastasis from the responder (**F**, arrow), shows no interval growth compatible with a sustained response.

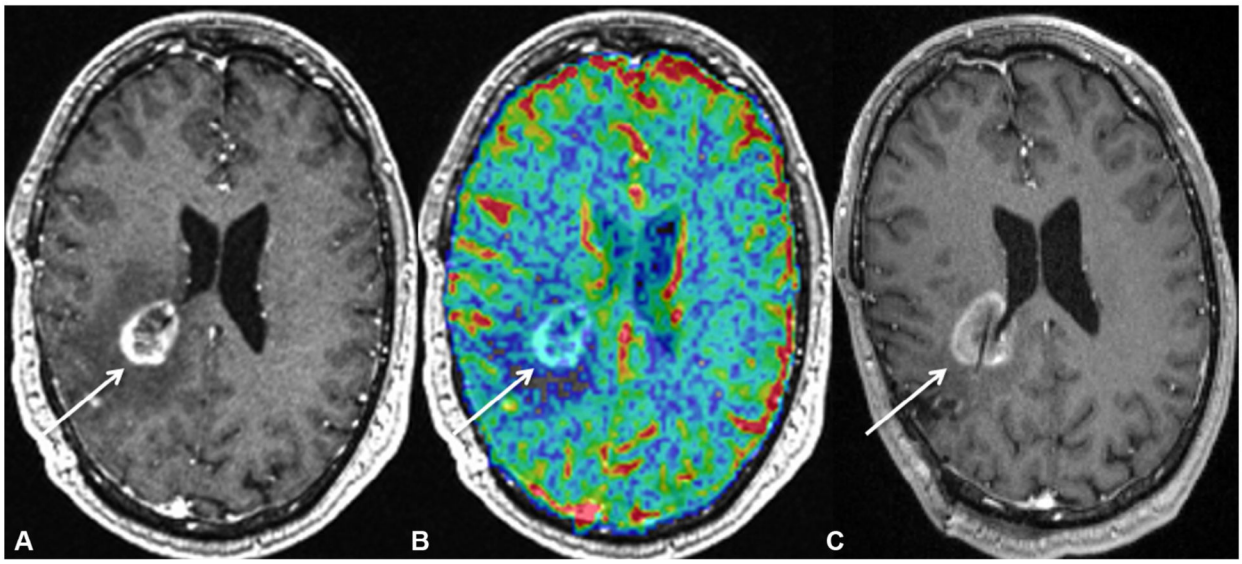

Fig. 7.6.

Perfusion imaging can help distinguish true from pseudoprogression. This patient with a history of brain metastases treated with radiation therapy developed a new ring-enhancing lesion on postcontrast T1-weighted images (**A**) adjacent to the right lateral ventricle. Low relative cerebral blood volume (**B**) was compatible with treatment effect rather than tumor recurrence and this was confirmed on biopsy (**C**). The patient subsequently underwent magnetic resonance imaging-guided laser ablation of this lesion with improved symptomatology.

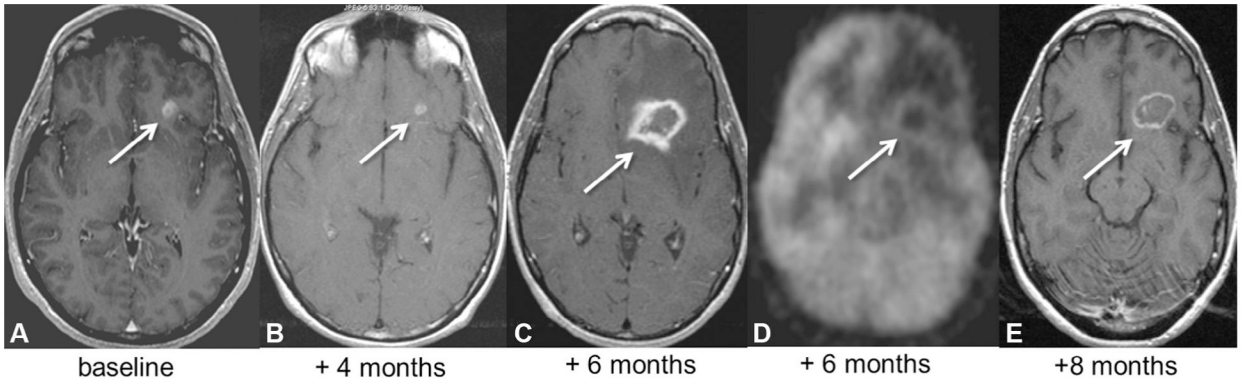

Fig. 7.7.

Potential added value of positron emission tomography (PET) imaging to help diagnosis radiation necrosis. Postcontrast T1-weighted images depict a left frontal-lobe lung carcinoma metastasis (arrows). The small lesion at baseline (time of stereotactic radiosurgery, **A**) appears to diminish slightly in size by 4 months posttreatment (**B**). However, the lesion is much larger in the follow-up scan 2 months later (**C**), but 18-fluorodeoxyglucose (FDG) PET (**D**) at that time demonstrated little tracer uptake, consistent with radiation necrosis rather than tumor progression. Subsequent imaging (**E**) shows the lesion (without additional treatment) beginning to regress, compatible with radiation necrosis.

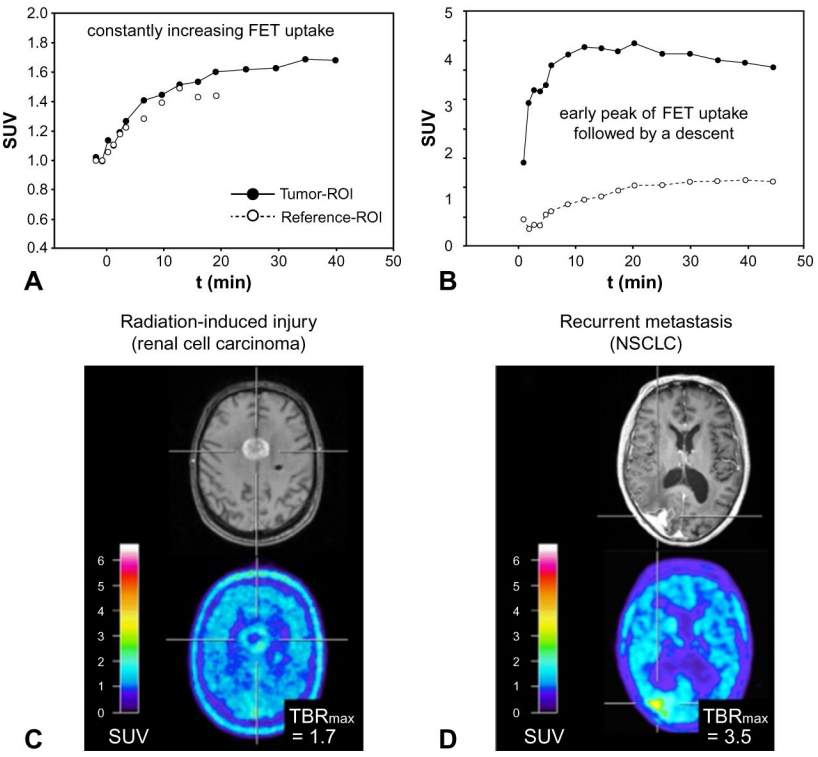

Fig. 7.8.

Time–activity curves may add value to static O-(2-[^{18}F]fluoroethyl)-L-tyrosine (FET)-positron emission tomography (PET) images for the identification of metastases versus treatment effect. Radiation injury mimicking tumor recurrence (**C**) exhibits increasing FET uptake **(A)**, whereas recurrent tumor (**D**) shows an increase followed by a decline in FET uptake (**B**). *NSCLC*, nonsmall cell lung cancer; *ROI*, region of interest; *SUV*, standardized uptake value. (Reproduced from Galldiks N, Langen KJ, Pope WB (2015) From the clinician's point of view – what is the status quo of positron emission tomography in patients with brain tumors? Neuro Oncol 17: 1434–1444, with permission from Oxford University Press.)

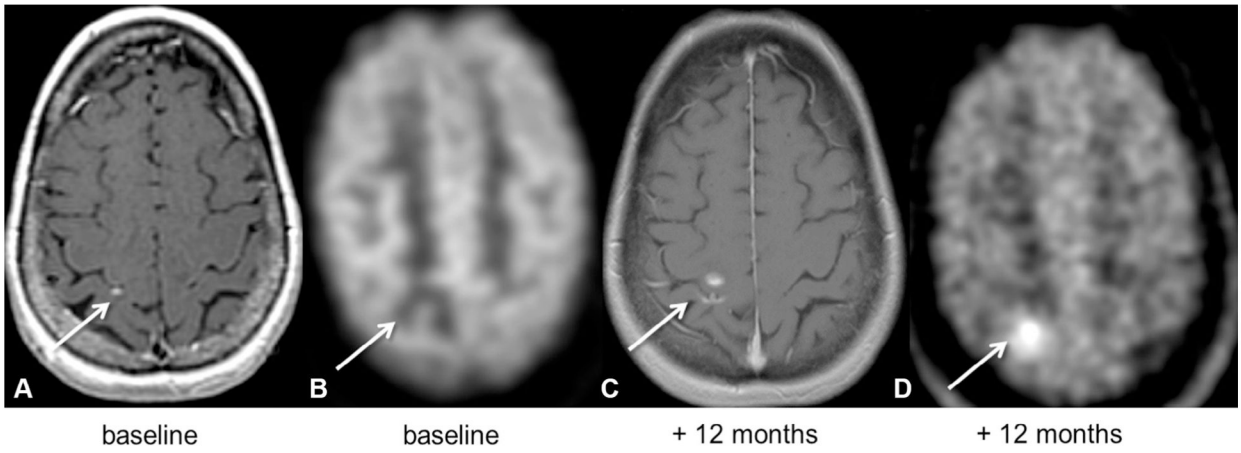

Fig. 7.9.

Potential advantage of amino acid positron emission tomography (PET) in identifying tumor recurrence. A patient with a history of successfully treated thyroid brain metastasis with a remnant punctate focus of enhancement present on postcontrast T1-weighted images (**A**, arrow) in the right central sulcus region. This lesion did not show tracer uptake on 18-fluorodeoxyglucose (FDG) PET (**B**, arrow), but high cortical background activity, as typically seen in FDG PET, reduces sensitivity for small lesions. One year later the patient developed increased enhancement in the region (**C**, arrow), which was thought to represent either recurrence or a radiation-induced cavernous malformation. 3,4-Dihydroxy-6-[^{18}F]-fluoro-L-phenylalanine (FDOPA) PET (**D**, arrow) showed the lesion to have high tracer uptake, compatible with recurrence, which was subsequently confirmed at surgery. Note the reduced background cortical activity of FDOPA PET (**D**) compared to FDG PET (**B**).

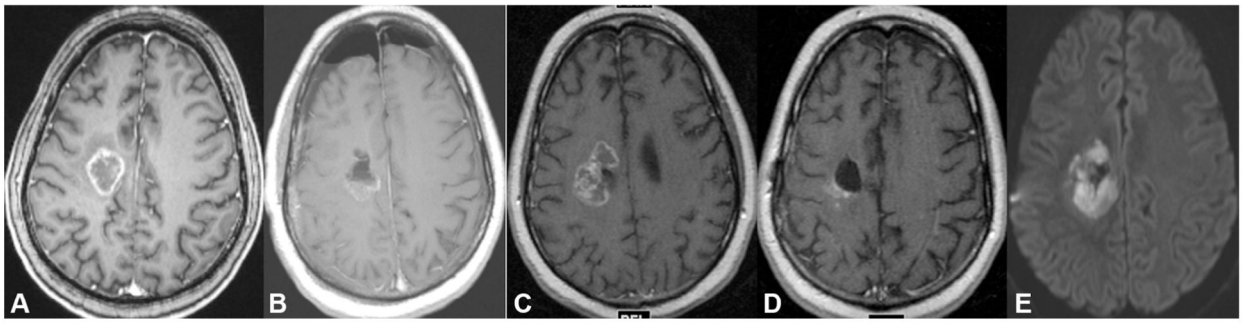

Fig. 7.10.

Effects of bevacizumab treatment on radiation necrosis. A patient with a cerebral testicular metastasis visible as a ringenhancing lesion on postcontrast T1-weighted images (**A**) was treated with resection (**B**) followed by radiation therapy. Subsequently the patient became symptomatic and follow-up imaging showed increased enhancement around the resection cavity (**C**). This was thought to represent radiation necrosis and the patient was treated with bevacizumab with reduction in enhancement (**D**) and reduced symptomatology. However the patient's symptoms returned and he was found to have a diffusion-restricted lesion around the resection cavity (**E**), which was confirmed to be radiation necrosis after a second surgery. The development of persistent diffusion-restricted lesions associated with radiation necrosis also has been described in patients with high-grade glioma treated with chemoradiation therapy followed by bevacizumab.

Table 7.1

Advanced/physiologic magnetic resonance imaging applications and associated biomarkers

Technique	Biomarker	Correlation
Diffusion-weighted imaging (DWI)	Apparent diffusion coefficient	Cellularity, cytotoxic and vasogenic edema
Diffusion tensor imaging (DTI)	Fractional anisotropy, mean diffusivity	Disruption of white-matter tracts
Dynamic susceptibility contrast (DSC)	Relative cerebral blood volume Mean transient time	Angiogenesis, vascular proliferation
Dynamic contrast-enhanced (DCE)	Contrast transfer coefficient (Ktrans)	Vascular permeability
Arterial spin labeling (ASL)	Cerebral blood flow	Vascularity